Volcanic Influence on Atmospheric Sulfur Cycle in 2.7 Ga inferred from Multiple Sulfur Isotope Record of Pyrite Nodules in Black Shales from Nimbus, Western Australia

by

Zhe Zhang

A thesis submitted in partial fulfillment of the requirements for the degree of

Master of Science

Department of Earth and Atmospheric Sciences
University of Alberta

Abstract

Sulfur isotope compositions of Archean sulfide and sulfate minerals show mass-independent fractionation (S-MIF) signatures, which are characterized by non-zero $\Delta^{33}S$ and $\Delta^{36}S$ values. Producing the Archean S-MIF signal requires an O_2-free atmosphere where broad-band UV radiation can penetrate to photolyze volcanic SO_2. Transfering and preserving the S-MIF signal to sediments also requires a reducing surface environment in which the dissociated SO_2 products (i.e., sulfide and sulfate) will not be oxidized and re-homogenized. In general, the Archean S-MIF indicates an extremely low oxygen level in the Archean atmosphere.

Most Archean sulfide minerals have $\delta^{34}S$ and $\Delta^{33}S$ values falling in a well-defined linear relationship with a positive $\Delta^{33}S/\delta^{34}S$ slope (around 0.9), which is named as the "Archean Reference Array" (ARA). However, a negative correlation between $\delta^{34}S$ and $\Delta^{33}S$ values has also been recently reported from the sulfide minerals in the 3.2 Ga Mapepe Formation, South Africa (Philippot et al., 2012). This anomaly was hypothesized to be the result of some different photolytic mechanism attributed to the shielding effect of volcanic aerosols during periods of intensive sub-aerial volcanic emissions, and was consequently named as the "Felsic Volcanic Array" (FVA).

To test the volcanic effect on atmospheric sulfur cycle in the Archean, Li et al. (2017) examined the multiple sulfur isotope compositions of pyrite nodules from the Joy Lake Sequence in the Superior Province with an age of 2.7 Ga, which was a peak time in Earth's Archean Eon for continental crust growth associated with intensive volcanic eruptions. The isotopic results of the pyrite nodules in the Joy Lake Sequence show a pattern very similar to FVA, suggesting a potential volcanic effect on the sulfur cycle in 2.7 Ga. However, the spatial scale of the volcanic effect is still not well constrained. To address this question, in particular to examine whether the

multiple sulfur isotopic signature with volcanic effect was only limited to local or expanded to a global scale of occurrence, we carried out high-resolution, *in-situ* multiple sulfur isotopic analysis of pyrite nodules from the 2.7 Ga Nimbus volcanic-hosted massive sulfide (VHMS) deposits in West Australia.

We used EPMA (for major and minor elements) and SIMS (for multiple sulfur isotopes) techniques to carefully characterize large diagenetic pyrite nodules, as well as fine-grained secondary hydrothermal pyrite grains disseminated in quartz veins, in the same samples from the Nimbus deposit. The results indicate that diagenetic pyrite nodules display elemental and isotopic patterns distinct from hydrothermal pyrite, indicating that the primary sulfur isotopic signatures of diagenetic pyrite nodules have not been geochemically altered by secondary hydrothermal alteration.

The Nimbus pyrite nodules show obvious isotopic zonation patterns with abrupt isotopic shift from core to rim regions. The cores are characterized by relatively low $\Delta^{33}S$ values (-0.6‰ to 1.0‰) and relatively high $\delta^{34}S$ values (-0.2‰ to 2.7‰), whereas the rims are characterized by higher $\Delta^{33}S$ values (2.1‰ to 3.4‰) and lower $\delta^{34}S$ values (-1.4‰ to 0.8‰). The multiple sulfur isotopic signatures of pyrite nodules suggest variable sulfur sources contributed to pyrite nodule formation. The cores of the pyrite nodules were derived from a mixture of seawater sulfate, submarine volcanic/hydrothermal sulfur, and elemental sulfur with ARA-like isotopic features from the commonly seen photochemical processes in the Archean. In contrast, the inner rims of pyrite nodules show a significant mass contribution from elemental sulfur derived from FVA-like elemental sulfur. This suggests a strong impact of volcanic activities on the atmospheric chemistry in the region, which resulted in a different S-MIF signature. The outer rims of the pyrite nodules show a progressive change from FVA-like to ARA-like isotopic patterns, again

implying a recovery of atmospheric chemistry from volcanic disturbance to the Archean background during the late stage of the pyrite growth.

A compilation of multiple sulfur isotope data of 2.7 Ga pyrite nodules from localities close to Nimbus shows that similar isotopic shift toward FVA-like elemental sulfur source can be clearly identified during the growth of pyrite nodules in sites extending for 300 km from the deposit. This suggests that Archean atmospheric environment could be very sensitive (both in effect and recovery) to volcanic activities at least at a regional scale.

Preface

Samples were provided by Dr. Steven Philip Hollis, University College Dublin. I'm responsible for sample selection, preparation, data collection and data analysis for this study.

Thin sections were prepared in the Thin Section Laboratory at the University of Alberta with help from Martin Von Dollen.

Multiple sulfur isotope analysis was carried out at the Canadian Centre for Isotopic Microanalysis (CCIM), University of Alberta, with help from Dr. Richard Stern and Dr. Long Li.

Elemental analysis was carried out at the Electron Microprobe Laboratory, University of Alberta, with help from Dr. Andrew Locock.

Acknowledgement

Firstly, I would like to thank my supervisor, Dr. Long Li. I appreciate his vast knowledge, guidance, and contributions of time and ideas. Thanks for his patience and support throughout the entire master period.

Secondly, I would like to thank my colleges, Jianghanyang Li, Kan Li, Yuying Deng and Yingzhou Li, for their encouragement and exchanges of knowledge and skills during the graduate program.

Last but not the least, I would like to thank my family and friends for being supportive throughout my years of study.

This research is funded by Natural Sciences and Engineering Research Council-Discovery Grant to Long Li.

Table of Content

List of Figures

List of Tables

1. Introduction

1.1. Multiple sulfur isotopes and mass independent fractionation

Sulfur has four stable isotope isotopes (^{32}S, ^{33}S, ^{34}S, and ^{36}S) and can give three isotopic ratios. In general, geological and biological processes are associated with significant sulfur isotope fractionations in all four isotopes, but the three ratios follow a mass-dependent fractionation (S-MDF) rule, which can be expressed as $\delta^{33}S = [(1+ \delta^{34}S/1000)^{0.515}-1]$ and $\delta^{36}S = [(1+ \delta^{34}S/1000)^{1.90}-1]$, in which $\delta^{3x}S = 1000 \times ({}^{3x}R_{Sample}/{}^{3x}R_{Standard} - 1)$; ${}^{3x}R = {}^{3x}S/{}^{32}S$; x = 3, 4, or 6; Standard is the Vienna-Canyon Diablo Troilite.

The study of multiple sulfur isotopes and their fractionation features in the last two decades, however, has demonstrated that the Archean sulfur can deviate from S-MDF and show sulfur mass-independent fractionation (S-MIF). The S-MIF is expressed by non-zero $\Delta^{33}S$ (= $\delta^{33}S - 1000 \times [(1+ \delta^{34}S/1000)^{0.515}-1]$) and $\Delta^{36}S$ (= $\delta^{36}S - 1000 \times [(1+ \delta^{34}S/1000)^{1.90}-1]$) values. In 2000, Farquhar and colleagues, for the first time, reported S-MIF in Archean sedimentary samples (Farquhar et al., 2000).

1.2. Multiple sulfur isotope signatures of Archean minerals and corresponding fractionation mechanism.

Numerous studies have repeatedly shown that, besides a negative linear trend (with a slope of ~ -1) on the $\Delta^{36}S$ versus $\Delta^{33}S$ diagram (Ono et al., 2003; Kaufman et al., 2007; Ono, 2009), most of the Archean sulfide and sulfate minerals have multiple sulfur isotopic values also falling in a narrow area along a positive linear trend (with a slope of ~ 0.9) on the $\Delta^{33}S$ versus $\delta^{34}S$ diagram, which is termed as the "Archean Reference Array" (ARA) (Figure 1). The ARA is interpreted to be the result of mixing between elemental sulfur (e.g., S_8) and sulfate SO_4^{2-} (Ono

et al., 2003), which are two major products of photodissociation of volcanic SO_2 in the atmosphere. Experimental investigations (e.g., Farquhar et al., 2001) show that photodissociation of SO_2 can produce elemental sulfur (S_8) with positive $\Delta^{33}S$ and sulfate (SO_3) with negative $\Delta^{33}S$. Modeling by Pavlov and Kasting (2002) suggests that a maximum threshold of 10^{-5} of the present atmospheric level of O_2 is required for the production and survivor of the S-MIF signals in the Archean atmosphere. Accordingly, the Archean S-MIF signal in geological records implies an O_2-free atmosphere in the Archean.

So far, despite a general consensus that the Archean S-MIF signal was produced by photochemical effects from UV radiation of volcanic SO_2 in the atmosphere (Farquhar et al., 2001; Ono et al., 2003), the detailed mechanism to produce S-MIF is still unclear. The interpretation of Archean S-MIF records has relied heavily on knowledge from both experimental and theoretical examinations of photochemical effects on multiple sulfur isotopes in response to UV radiation at different wavelength bands. As noted above, experiments carried out by Farquhar et al. (2001) using single-wavelength UV radiation reproduced the Archean S-MIF signal. However, the solar UV radiation covers a continuous wavelength of spectra, and the main SO_2 absorption spectra are quite broad at both 190-220 nm and 250-330 nm (Heicklen et al., 1980). Accordingly, other researchers argued that a broadband light source that covers the entire SO_2 absorption spectra should be more reasonable to simulate the solar radiation effects on SO_2. Later experiments (e.g., Masterson et al., 2011; Whitehill and Ono, 2012) have used a broadband light source, but with extremely high concentration of SO_2 as reactant gas (pure SO_2). These experiments could not reproduce the Archean S-MIF signature. More recently, Ono et al. (2013) conducted further experiments with low SO_2 concentration as reactant (as low as 0.1mbar by mixing with N_2), but these experiments were still not able to reproduce the Archean S-MIF

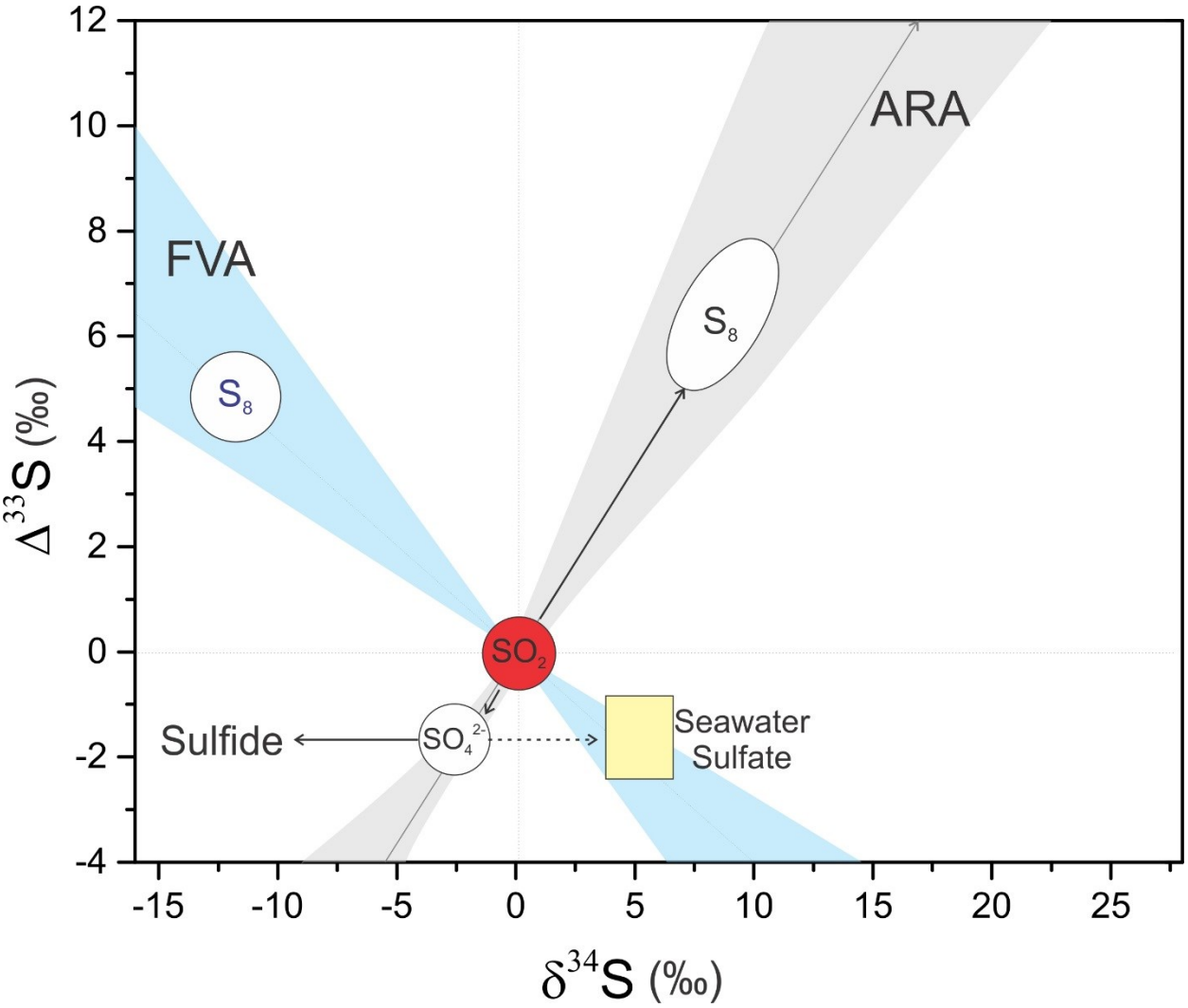

Figure 1. $\Delta^{33}S$-$\delta^{34}S$ diagram illustrates the commonly seen Archean Reference Array (in grey) and the less common Felsic Volcanic Array (blue).

signature. Meanwhile, carbonyl sulfide (OCS) was proposed as an important component in the Archean atmosphere that could affect the atmospheric sulfur cycle (Ueno et al., 2009). Following this proposal, Endo et al. (2016) conducted photochemical experiments by mixing SO_2 with CO as the reactant to produce CO_2 and OCS. This experimental study successfully reproduced the Archean $\Delta^{36}S/\Delta^{33}S$ signature (from -0.9 to -1.5), yet the slope of the $\Delta^{33}S/\delta^{34}S$ signature (~ 0.13) is still markedly different from that of the ARA (~ 0.9).

In summary, there still exists a significant discrepancy between the experimental results and the geological S-MIF records ─ experimental conditions and/or starting material employed in the experiments that reproduced the Archean S-MIF signature were considered to be unrealistic, whereas experimental conditions close to the speculated Archean atmospheric conditions have not been able to reproduce the Archean S-MIF record.

Nevertheless, some of the experimental studies do provide some valuable insights into the understanding of the mechanism behind the SO_2 photolysis. Endo et al. (2016) summarized three possible mechanisms for the cause of S-MIF: (1) wavelength-dependent isotopic effect in SO_2 photolysis (2) SO_2 self-shielding effect, and (3) SO_2 photoexcitation, which are briefly described below.

(1) Wavelength-dependent isotope effect in SO_2 photolysis:

Wavelength-dependent energy from UV radiation can dissociate different SO_2 isotopologues at different rates, which can result in S-MIF. To predict such an isotopic effect, it is crucial to have precise and accurate UV absorption spectra of SO_2 isotopologues. Danielache et al. (2008) first measured the absorption spectra of three SO_2 isotopologues (i.e., $^{32}SO_2$, $^{33}SO_2$, $^{34}SO_2$) by laboratory experiments. Using Danielache's results, some studies have applied atmospheric modeling to infer the Archean

atmospheric chemistry based on the Archean S-MIF records (Ueno et al., 2009; Claire et al., 2014). However, the results of Danielache et al. (2008) have been called into question for the inconsistency with the other experimental results (Whitehill and Ono, 2012) and large error. Later, Endo et al. (2015) have improved Danielache's experiments (error reduced from 156‰ to 9‰) and obtained high-resolution absorption spectra for four SO_2 isotopologues (i.e., $^{32}SO_2$, $^{33}SO_2$, $^{34}SO_2$, $^{36}SO_2$). The calculation based on the new spectra reached a $\Delta^{33}S/\delta^{34}S$ slope around 1 and a $\Delta^{36}S/\Delta^{33}S$ slope around -0.9, successfully reproducing the Archean signal. However, these theoretical estimates are presumed to occur under the optically thin condition without any other effect (e.g., self-shielding or shielding by other gases) (Endo et al., 2016), which is difficult to achieve in reality and have not yet been investigated experimentally.

(2) Self-shielding effect:

Self-shielding is another mechanism that can produce S-MIF signals. The energy from UV light is gradually absorbed and decreased when going through the SO_2 gas, which leads to different photodissociation rate for SO_2 isotopologues, and subsequently generates S-MIF (Lyons, 2007; Lyons, 2008). This self-shielding effect is common and particularly effective at high SO_2 partial pressure conditions. This effect was first proposed by Lyons (2007) using theoretical calculations based on *ab-initio* calculated spectra. In tandem with theoretical estimates, experiments by Whitehill and Ono (2012) and Ono et al. (2013) have further produced elemental sulfur with different $\Delta^{33}S$ values dependent on the partial pressure of SO_2 in reactants during photolysis. However, the self-shielding effect based on *ab-initio* calculated spectra (Lyons, 2007) and laboratory

experiments (Whitehill and Ono, 2012; Ono et al., 2013) gave $\Delta^{36}S/\Delta^{33}S$ ratios lower than -3, inconsistent with the Archean record ($\Delta^{36}S/\Delta^{33}S$ = -0.9).

(3) SO_2 photoexcitation:

Experimental investigations have suggested that the wavelength-dependent isotope effect is not pronounced for wavelength above 250 nm (Whitehill, 2013). Instead, at higher wavelengths (e.g., 250-350 nm), photoexcitation occurs when energy from UV radiation induces SO_2 into different excited states. The transition between different excited states of SO_2 could cause the S-MIF (Whitehill, 2013). However, SO_2 photoexcitation experiments have only produced a positive $\Delta^{36}S/\Delta^{33}S$ slope ($\Delta^{36}S/\Delta^{33}S$= +1.1 to 2.2) (Whitehill, 2013), very different to the Archean geological records characterized by negative $\Delta^{36}S/\Delta^{33}S$ slope of ~ -1.

Besides these photochemical effects on SO_2, some other mechanisms have also been proposed to explain the S-MIF. For example, based on theoretical calculations, Sarka et al. (2017) suggested that photolysis of S_2 could produce S-MIF signal. More complicated isotopic effects associated with a series of photochemical reactions from $S \rightarrow S_2 \rightarrow S_4 \rightarrow S_8$ have also been proposed as potential candidates to produce S-MIF (Babikov, 2017; Babikov et al., 2017). But none of these has been demonstrated to be consistent with the Archean geological records yet. In laboratory experiments, Watanabe et al. (2009) observed non-zero $\Delta^{33}S$ values through thermochemical reduction of sulfate (TSR) and suggested TSR as another possible mechanism to interpret the Archean S-MIF record. However, Oduro et al. (2011) have re-interpreted those anomalous $\Delta^{33}S$ value from TSR as a magnetic isotopic effect which can only shift $\Delta^{33}S$ but not $\Delta^{36}S$ values.

Overall, the discrepancies in the S-MIF signal between geological records and experimental results as well as theoretical calculation still remain. Further studies are still needed to unravel the Archean S-MIF mystery.

An interesting new discovery with regard to the Archean S-MIF signal is a $\Delta^{33}S$ - $\delta^{34}S$ trend with a negative slope (different to the major ARA trend with positive slope) in the sulfide minerals from volcanic ash layers in the 3.2 Ga Mapepe Formation in South Africa (Philippot et al., 2012). This anomalous negative trend has been attributed to a different photochemical effect on SO_2 photolysis due to the intensive volcanic emission which shifted the atmospheric chemistry for a short time period, and consequently named as the "Felsic Volcanic Array" (FVA) (Philippot et al., 2012; also see Figure 1). Later, Muller et al. (2016) have confirmed this anomalous photochemical effect from the Archean barite in the 3.49 Ga Dresser Formation, Pilbara Craton, Western Australia and the 3.2 Ga Mapepe Formation, South Africa.

Currently, there is a strong debate in the S-MIF community on whether this negative trend is related to volcanic effect. If this anomalous photochemical effect was related to intensive volcanic emission, it is expected to be observed in the 2.7 Ga geological records, because 2.7 Ga was a peak period of continental crust growth with intensive volcanic activities in the Archean (Condie, 1998). Li et al. (2017) have first reported an FVA-like S-MIF signature in the 2.7 Ga Joy Lake sequence (Superior Province), which was deposited in an environment close to volcanic arc. However, a similar S-MIF signature was not observed in other 2.7 Ga sediments previously reported (Ono et al., 2003; Ohmoto et al., 2006; Farquhar, 2007; Domagal-Goldman et al., 2008; Thomazo et al., 2009; Zerkle et al., 2012; Jamieson et al., 2013; Kurzweil et al., 2013; Marin-Carbonne et al., 2014; Gregory, 2015; Izon et al., 2015; Williford et al., 2016). This raises questions about the spatial and temporal scales of the volcanic effect. Li et al. (2017)

speculated that the volcanic effect may be short-lived and local in scale, and thus not recorded in distal sediments. This is possible because a large volume of volcanic gas shielding is a prerequisite for the FVA signature, and intensive SO_2 emission generally occurs in specific tectonic settings (i.e., subduction zone or rift zone). Thus, it is more likely that the FVA-like S-MIF would be closely associated with these specific tectonic settings.

To examine the possible occurrence of this volcanic effect in other localities and further constrain the spatial and temporal scales of the volcanic effect, we investigated samples from the Nimbus VHMS deposits (West Australia), which is suggested to be formed at the margin of a ~2.7 Ga paleo-rift zone in a period of intense volcanism (Hollis et al., 2017). High-resolution *in-situ* chemical and isotopic analyses (by SIMS and EPMA) were conducted on large pyrite nodule grains and fine-grained secondary hydrothermal pyrites grains to carefully identify the primary diagenetic sulfur isotope signature from the late metamorphic effect.

2. Geological setting and samples

Our study targets are drill core samples from the Nimbus mine (17 km east-southeast of Kalgoorlie). The mine is located in the Boorara Domain of the Kalgoorlie Terrane within the Eastern Goldfields Superterrane of the Yilgarn Craton, West Australia (Figure 2A). The Kalgoorlie Terrane is bounded by the Ockerburry fault system in the east and the Ida fault system in the west (Swager et al., 1992; Swager, 1997). The regional geological units of Kalgoorlie Terrane can be divided into the 2690-2660 Ma upper Kalgoorlie Sequence (Krapež and Hand, 2008) and the 2720-2690 Ma lower Kambalda Sequence (Beresford et al., 2005). Based on zircon U-Pb dating results of 2703 ± 5 Ma and 2702 ± 4 Ma from the host dacite of the Nimbus deposits (Hollis et al., 2017), these deposits are considered to be part of the Kambalda

Sequence, which comprises komatiitic and tholeiitic mafic-ultramafic rocks with minor felsic volcanics and sediments (Campbell et al., 1989; Swager et al., 1992).

The geodynamic history of the Eastern Goldfields Superterrane is still under debate. Previous studies have suggested that Kalgoorlie Terrane was formed in a back-arc extensional setting associated with the west-dipping subduction around 2715-2690 Ma (Barley et al., 1989; Krapez, 1997; Morris and Witt, 1997; Barley et al., 2008; Czarnota et al., 2010). In contrast to the subduction hypothesis, some other researchers suggested it as part of the West Kurnalpi rift zone (Archibald et al., 1978; Groves and Batt, 1984; Hallberg, 1986; Said et al., 2010; Huston et al., 2014; Hollis et al., 2017). In addition, some researchers proposed that the Kambalda Sequence was produced by an Archean mantle plume(Campbell and Hill, 1988; Campbell et al., 1989; Hill et al., 2011; Barnes and Van Kranendonk, 2014).

The Nimbus mine is considered to be a volcanic-hosted massive sulfide (VHMS) deposit within an Archean greenstone belt (Hollis et al., 2017). The lithology of the Nimbus deposits can be subdivided into three units: (1) upper polymict conglomerate, (2) middle basalt, and (3) lower quartz-feldspar porphyritic dacite (Figure 2C) (Hollis et al., 2017). The samples investigated in this study are from the upper polymict conglomerate unit. The polymict conglomerate is composed of dacite clasts and a graphitic matrix (Figure 3). The poorly-sorted but rounded characteristics of the clasts indicate a sub-aerial origin as an emergent dome or stratovolcano (Hollis et al., 2017). The depositional environment was interpreted as a shallow-water anoxic basin with debris flow from the sub-aerial shoreline (Hollis et al., 2017).

The rocks in Nimbus have been subjected to lower greenschist-facies metamorphism (Hollis et al., 2017). Hydrothermal alteration is evident in the Nimbus deposits, as shown

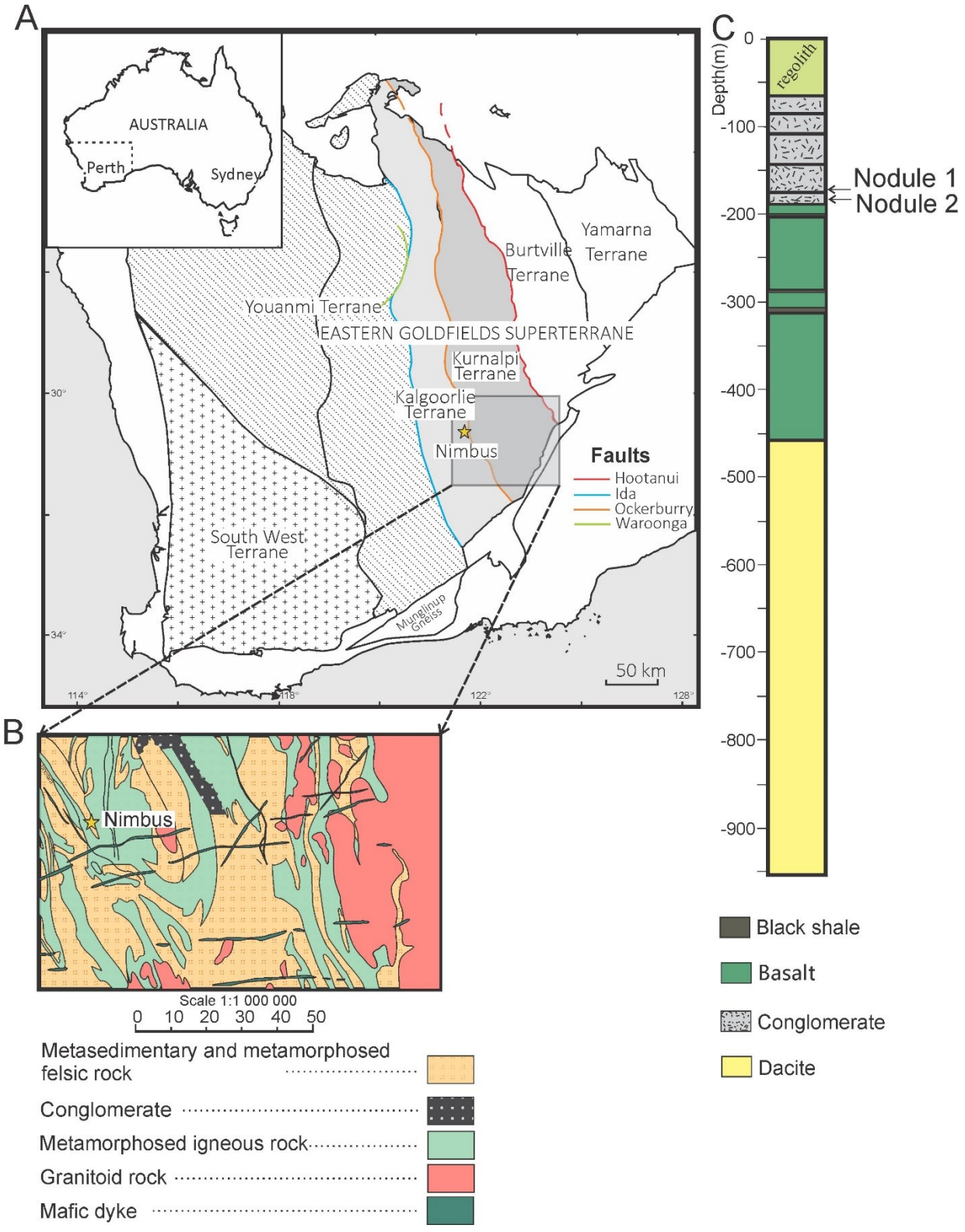

Figure 2. Geological map of the Nimbus area and drill core log information for NBDH010 (after Belford et al. 2015; Czarnota et al. 2010; Hollis et al. 2017 and 1:250000 geological map from Geological Survey of Western Australia).

by secondary mineral assemblages of quartz-sericite±carbonate in dacitic rocks and quartz-carbonate-chlorite in mafic rocks (Hollis et al., 2017; also see Figure 4).

Two organic-rich samples with abundant pyrite nodules were picked for petrographic investigation under the microscope. One pyrite nodule from each sample was selected based on morphology and size for detailed elemental and sulfur isotopic analyses. For comparison, small subhedral pyrite grains disseminated in the quartz veins around the pyrite nodules were also examined for elemental and sulfur isotope compositions.

3. Analytical method

3.1. Electron Probe Microanalysis (EPMA) analyses

The EPMA measurements and X-ray elemental maps were conducted by a Cameca SX100 microprobe with 5 tunable wavelength dispersive spectrometers (WDS) at the EPMA Laboratory, University of Alberta. The instrument has a 40^0 takeoff angle and was operated at a 20 keV accelerating voltage, a 20 nA beam current and a 2-micron beam diameters. The reference materials used for calibration are $KAlSi_3O_8$ (Itrongay sanidine) for Si, copper metal for Cu, cobalt metal for Co, synthetic gallium arsenide for As, iron disulfide (FeS_2) for Fe and S, and nickel for Ni. The counting time was 30 seconds for Si ka, Fe ka, 40 seconds for Co ka, Ni ka, Zn ka, 60 seconds for S ka, Cu ka, 80 seconds for As la, and 100 seconds for Ag la. The off peak counting time was 30 seconds for Si ka, Fe ka, 40 seconds for Co ka, Ni ka, Zn ka, 60 seconds for S ka, Cu ka, 80 seconds for As la, and 100 seconds for Ag la.

For pyrite nodules, the major and minor elemental analyses were carried out along a cross-grain traverse line that followed the isotopic analysis. The analyses were carried out on one spot every 20 μm distributed evenly along the selected traverses. For the small subhedral pyrite grains, major and minor elemental analyses were conducted on two spots close to each isotopic

analysis spot. Analytical uncertainty (2σ) is 0.19% for S, 0.15% for Fe, 0.01% for Co, 0.01% for Cu, and 0.01% for Ni. The detection limit at 99% confidence level is 0.013% for S, 0.014% for Fe, 0.014% for Co, 0.014% for Cu, and 0.013% for Ni.

Each pyrite nodule was also X-ray mapped for Si, S, Cu, Ag and Ni by EPMA-WDS using a fully focussed beam, a 3μm/pixel signal, a dwell time of 20 ms per pixel.

3.2. Secondary Ion Mass Spectrometry (SIMS) analyses

Sample preparation and secondary ion mass spectrometry (SIMS) analysis were carried out at the Canadian Centre for Isotopic Microanalysis (CCIM), University of Alberta. Pyrite nodules were cut out and cast into a 25-mm epoxy mount together with the CCIM pyrite reference materials (S0302A, S0329) and an Archean Ni-rich sulfide sample, and then cleaned, polished, and coated with 10 nm Au before examination on scanning electron microscopy (SEM) for detailed petrographic examination. SIMS analytical positions were selected on individual secondary subhedral pyrite grains which are disseminated in quartz veins. For pyrite nodules, the analytical positions were selected along a roughly straight line across the center on pyrite nodules, but sometimes shifted slightly to avoid the visible inclusion-bearing area.

Analysis of sulfur isotope ratios of $^{34}S/^{32}S$ and $^{33}S/^{32}S$ has been described in Li et al. (2017). The analysis in this study followed this method. In addition to the two isotopic ratios measured in Li et al. (2017), we also measured the third isotopic ratio, i.e., $^{36}S/^{32}S$. In brief, all four sulfur isotopes were measured by the IMS-1280 multi-collector ion microprobe, following methods described in Li et al. (2017). The primary beam using 20 keV $^{133}Cs^+$ ions was operated at ~1.5 nA current and ~10 μm diameter. All secondary ions were extracted by -10kV secondary

beam and collected by either Faraday cups (for ^{32}S, ^{33}S, and ^{34}S) or an electron multiplier at the H2 position (for ^{36}S).

Two internal pyrite reference materials S0302A and S0329 have been used to calibrate the measured results. Reference values for S0302A are $\delta^{34}S_{VCDT}$ = 0.0‰, $\Delta^{33}S$ = 0‰, and $\Delta^{36}S$ = 0‰ for S0302A, and $\delta^{34}S_{VCDT}$ = +3.3‰, $\Delta^{33}S$ = 0‰, and $\Delta^{36}S$ = 0‰ for S0329. The standard deviations of $^{33}S^{-}/^{32}S^{-}$, $^{34}S^{-}/^{32}S^{-}$, and $^{36}S^{-}/^{32}S^{-}$ ratios for S0302A were 0.05‰, 0.02‰, and 0.30‰ respectively. The total analytical uncertainties are 0.11‰ for $\delta^{34}S$, 0.09‰ for $\Delta^{33}S$, and 0.55‰ for $\Delta^{36}S$ at the 95% confidence level. An Archean Ni-rich chalcopyrite bearing homogeneous S-MIF signal was also tested for data quality control. The results gave wrong $\delta^{34}S$ values because of the matrix effect (different concentrations of Ni of pyrite) but identical $\Delta^{33}S$ and $\Delta^{36}S$ values to those measured by the conventional SF_6 method.

4. Results

4.1. Petrology and mineralogy

The samples in this study were selected from a long (921.1m) diamond drill core NBDH010 in the Nimbus mine. NBDH010 cuts through several stratigraphic strata as being illustrated in Figure 2C. Two hand samples were selected from the pyrite-rich conglomerates in the upper unit at depths of 170 m and 184.64 m, respectively. These conglomerates share two common features: (1) oval or rounded pyrite nodules surrounded by quartz pressure shadow or cut through by quartz veins, and (2) sub-rounded to rounded clasts of dacite and volcanic sandstone (arkose) in the matrix (Figure 3).

The dacitic clasts are sub-rounded to rounded but poorly sorted, distributed in the matrix but generally not in contact with pyrite nodules (Figure 3B). Under the microscope, the dacitic clasts display a porphyritic texture with plagioclase and quartz as phenocrysts in the fine

crystalline matrix (Figure 4C & D). The plagioclase has been partially altered to sericite by the hydrothermal fluid during later metamorphism. The small (~80 μm) anhedral to subhedral pyrite and sphalerite grains can be observed in quartz phenocrysts and matrix in the clasts (Figure 4C & D). But these small sulfide grains in the dacitic clasts are obviously different to the large pyrite nodules in the organic-rich matrix.

The volcanic sandstone clasts in the samples are mostly rounded in shape and mainly consist of coarse plagioclase and quartz grains (Figure 3A). Plagioclase grains are large and have been intensively altered to sericite (Figure 4E & F).

Abundant pyrite nodules ranging from less than 1 mm to >16 mm have been observed in these hand samples. The pyrite nodules are commonly associated with pressure shadow, which is filled with quartz and sericite (or muscovite) (Figure 4A & B). Euhedral to subhedral pyrite grains (up to 500 μm) occur in the pressure shadow. Small grains of disseminated pyrites (~ 2 μm) also spread out in the matrix of the conglomerate samples.

One nodule from each sample was selected for detailed elemental and isotopic investigations. Both nodules show obvious zonation patterns in the BSE images (Figures 5 & 6), with an inclusion-rich core and a relatively clean rim with a coarse bladed shape of radiating texture. Small secondary pyrite grains in subhedral shape are widespread in the pressure shadow, some even grew in contact with the rim of the large pyrite nodule gains (e.g., Figure 5). Some medium-size pyrite grains in the pressure shadow and graphitic matrix show irregular shapes with morphology very similar to pyrite nodules, likely are parts of pyrite nodules but have been broken or even dissolved to small relics.

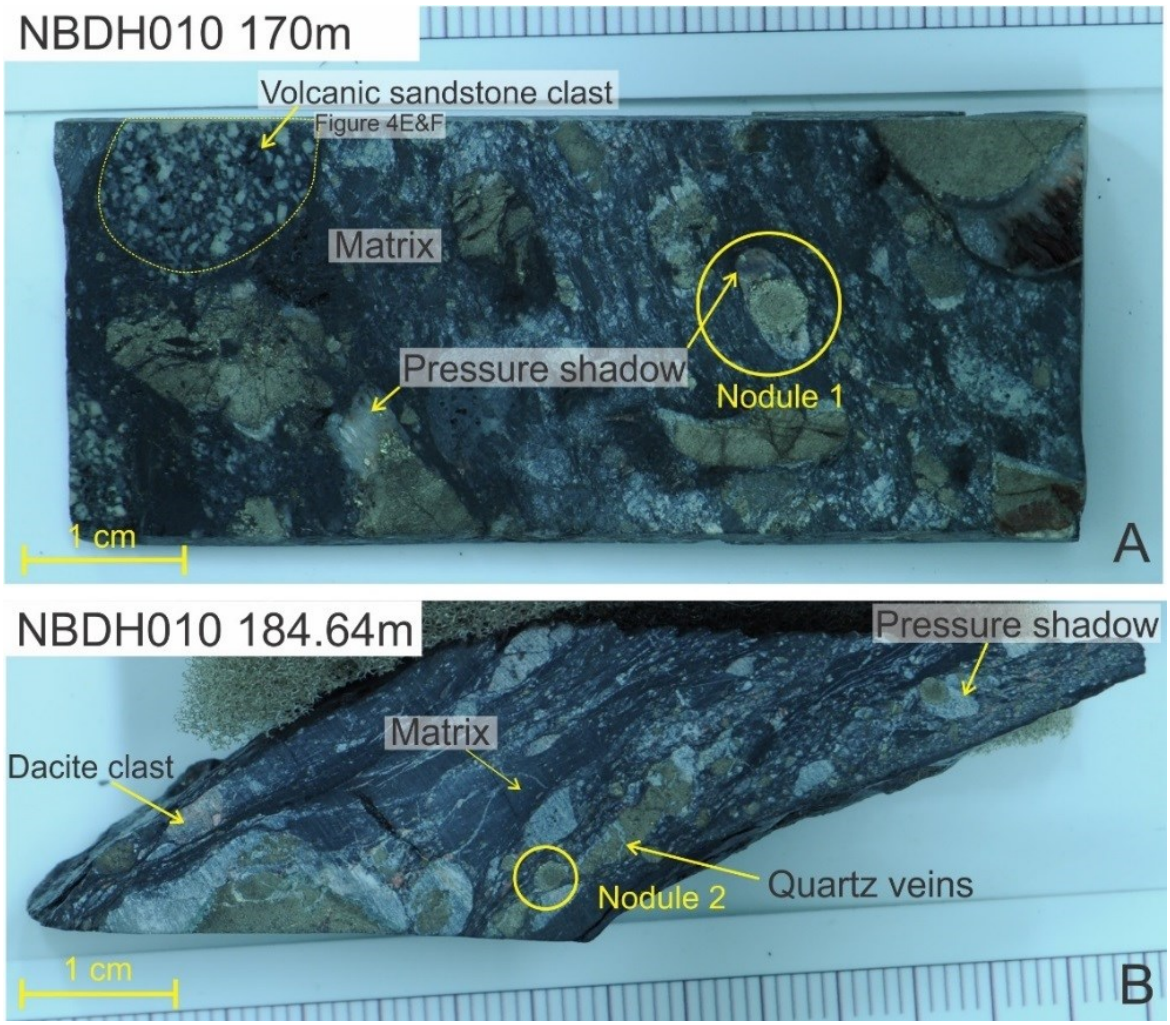

Figure 3. Photos of two polymict conglomerate hand samples for this study. Volcanic sandstone and dacitic clasts are rounded but poorly sorted in the matrix. Pressure shadows filled with quartz were developed around the pyrite nodules. Some large pyrite nodules have been cut through by quartz veins.

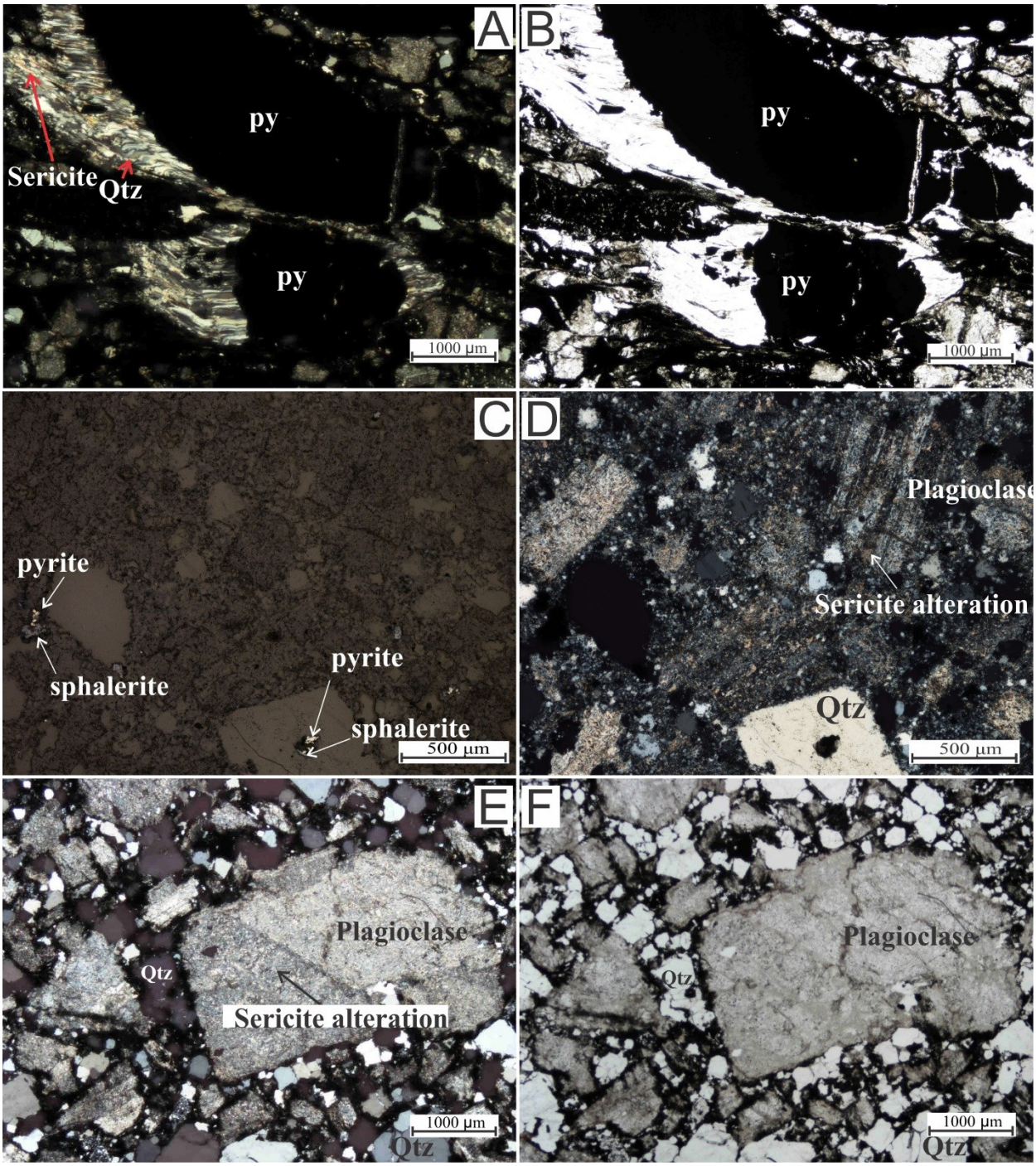

Figure 4. Cross-polarized light (XPL), plane polarized light (PPL), and reflected light microscopic images of thin sections of the two hand samples. A, B, E, and F belong to hand sample from 170 m. C & D belong to hand sample from 184.64 m. A & B show well-developed pressure shadow around pyrite nodules. The pressure shadow is filled with oriented quartz and sericite fibres, which indicate the extensional direction during deformation. C & D show that dacitic clasts have been altered by hydrothermal fluid with small (~ 80 µm) pyrite and sphalerite precipitation. E & F show volcanic sandstone clasts containing angular quartz grain and large plagioclase, which is partially altered to sericite.

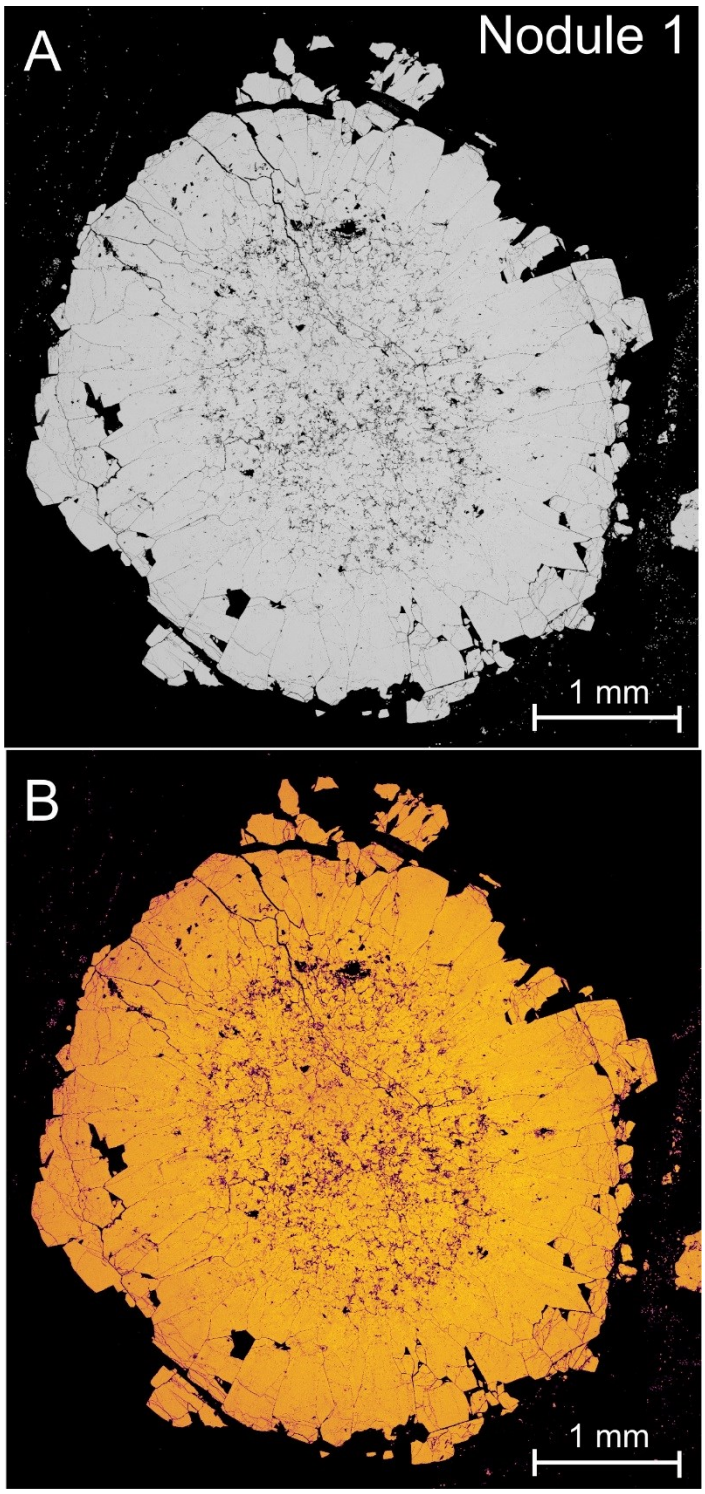

Figure 5. Backscatter electron image (BSE) of Nodule 1. A. True color grey scale image recorded by BSE. B. Colorized image from A using the software "ImageJ" from National Institutes of Health.

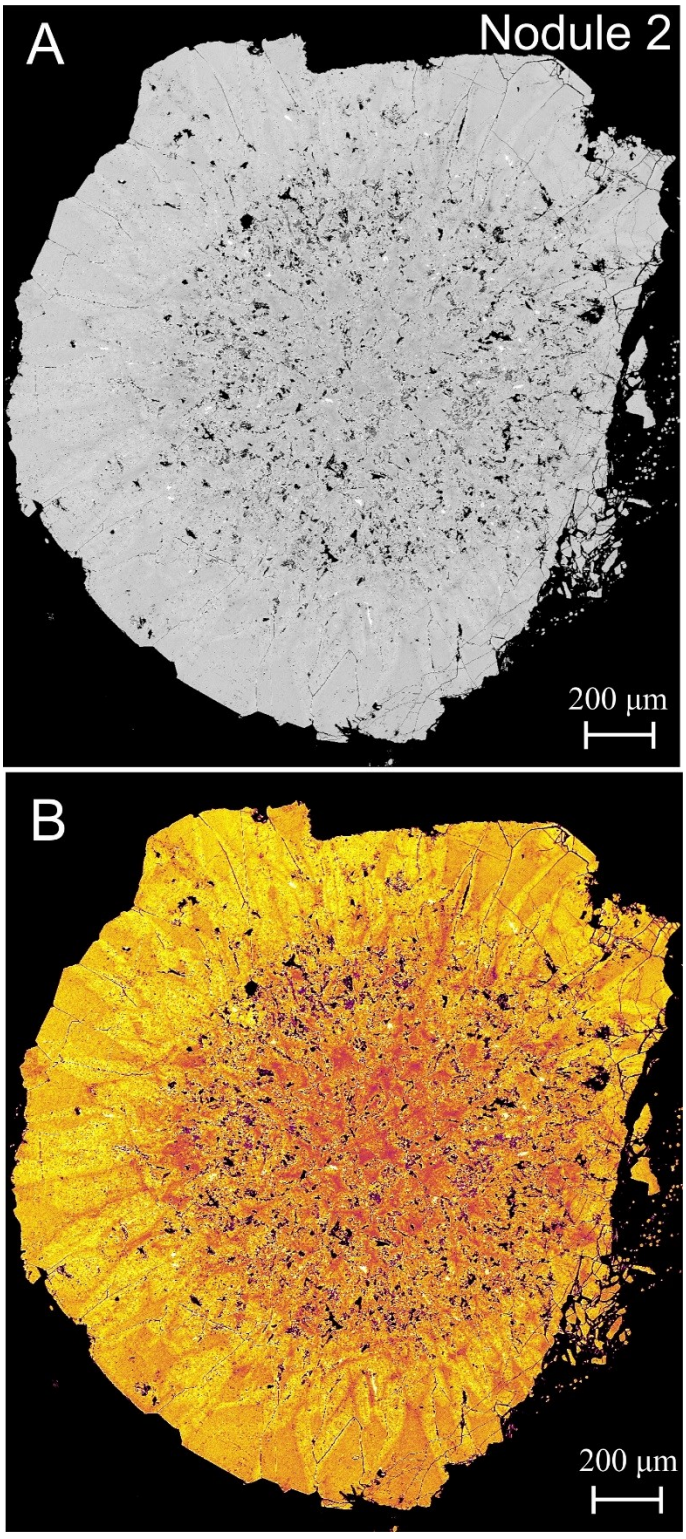

Figure 6. BSE image of Nodule 2. A. True color grey scale image by BSE. B. Colorized image shows clear zonation pattern.

4.2. Major and minor element composition of pyrite nodules

Major (Fe and S) and potential minor element concentrations including Si, Zn, Co, Ni, Cu, As and Ag were measured. However, Si, Zn, As and Ag concentrations are mostly under detection limits. Thus, only the data of Ni, Cu, Co, Fe, and S are presented here (Table 1).

4.2.1. Pyrite nodule

EPMA analysis across both selected pyrite nodule grains reveals similar characteristics in analytical totals and Ni profiles, but slightly different in Cu and Co concentrations between the two nodules (Figure 7).

The Fe and S concentrations and analytical totals display similar symmetrical zoning patterns in both nodules – higher in the rim and lower in the core (Figure 7A & B). From the core to the rim of Nodule 1, the concentration varies from 44.89% to 47.02% for Fe, from 50.34% to 54.05% for S, and from 95.59% to 101.09% for total elements. From the core to the rim of Nodule 2, the concentration varies from 45.36% to 46.07% for Fe, from 52.81% to 53.50% for S, and from 96.31% to 100.00% for total elements. The atomic S/Fe ratio of both nodules is 2.02 ± 0.02 (2σ, n = 100 for Nodule 1 and n = 50 for Nodule 2), demonstrating both nodules are in form of FeS_2 (pyrite).

In the minor element maps (Figure 8), Ni concentration shows two distinct zones in both nodules. The cores have relatively high Ni concentrations, varying from 0.04% to 0.14% (average: 0.10 ± 0.04‰, 2σ, n = 66) for Nodule 1, and from 0.13% to 0.36% (average: 0.22 ± 0.1%, 2σ, n = 18) for Nodule 2, respectively. In contrast, Ni concentrations in the rims are mostly below the detection limit (Figure 7C & D). Cu and Co concentrations display different features in the two pyrite nodule grains. Cu concentrations in Nodule 1 (Figure 7G) show a similar pattern with Ni concentration (Figure 7C) with relatively high concentrations in the core

but below the detection limit in the rim. Cu concentrations in Nodule 2 (Figure 7H) are mostly very low (around 0.02%) except a few random hot spots, which are related to discrete micro-scale inclusions (white dots in Figure 8). In contrast, Co concentrations are mostly below detection limit in Nodule 1, but show detectable values (0.02% to 0.08%; average: 0.04 ± 0.04%, 2σ, n = 18) in the core, and undetectable amount in the rim of Nodule 2 (Figure 7E & F).

4.2.2. Secondary subhedral pyrite disseminated in quartz veins/shadows

For comparison, the small secondary subhedral pyrite grains in pressure shadow (particularly some grains in contact with pyrite nodules; Figure 5) were also analyzed by EPMA for their major and minor element compositions. They have concentrations from 45.64% to 46.65% (average: 46.21 ± 0.22%, 2σ, n = 40) for Fe, from 53.20% to 54.02% (average: 53.80 ± 0.18%, 2σ, n = 40) for S, and from 99.85% to 101.54% (average: 100.93 ± 0.37%, 2σ, n = 40) for analytical totals. For minor elements, the secondary subhedral pyrite grains are characterized by high Ni concentration ranging from 0.02% to 0.12% (average 0.06 ± 0.03%, 2σ, n = 40), but low Cu and Co concentrations (both below detection limits).

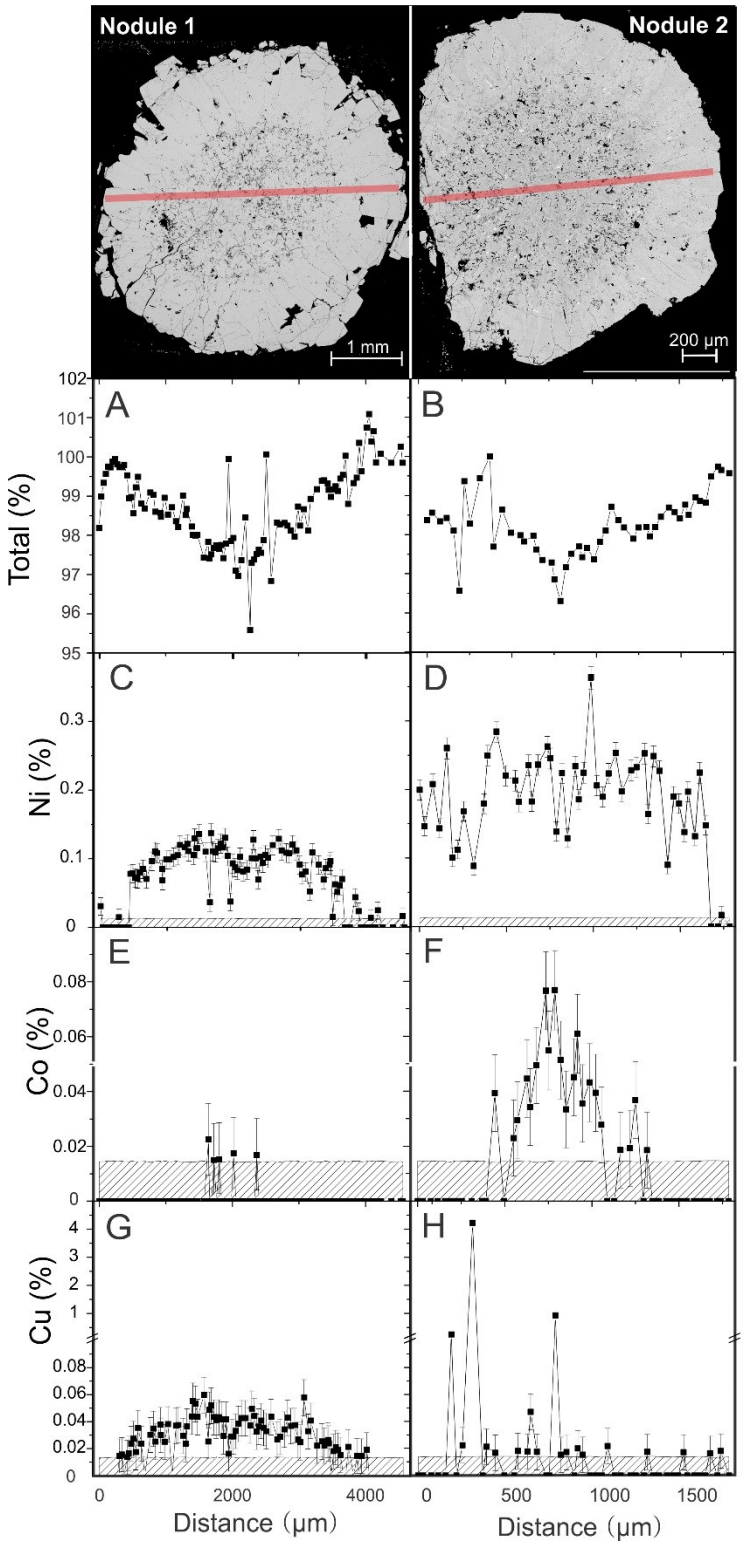

Figure 7. Variations of major and minor elements concentrations across pyrite nodules 1 and 2. The shaded areas represent the detection limits. The red lines mark the EPMA analytical positions.

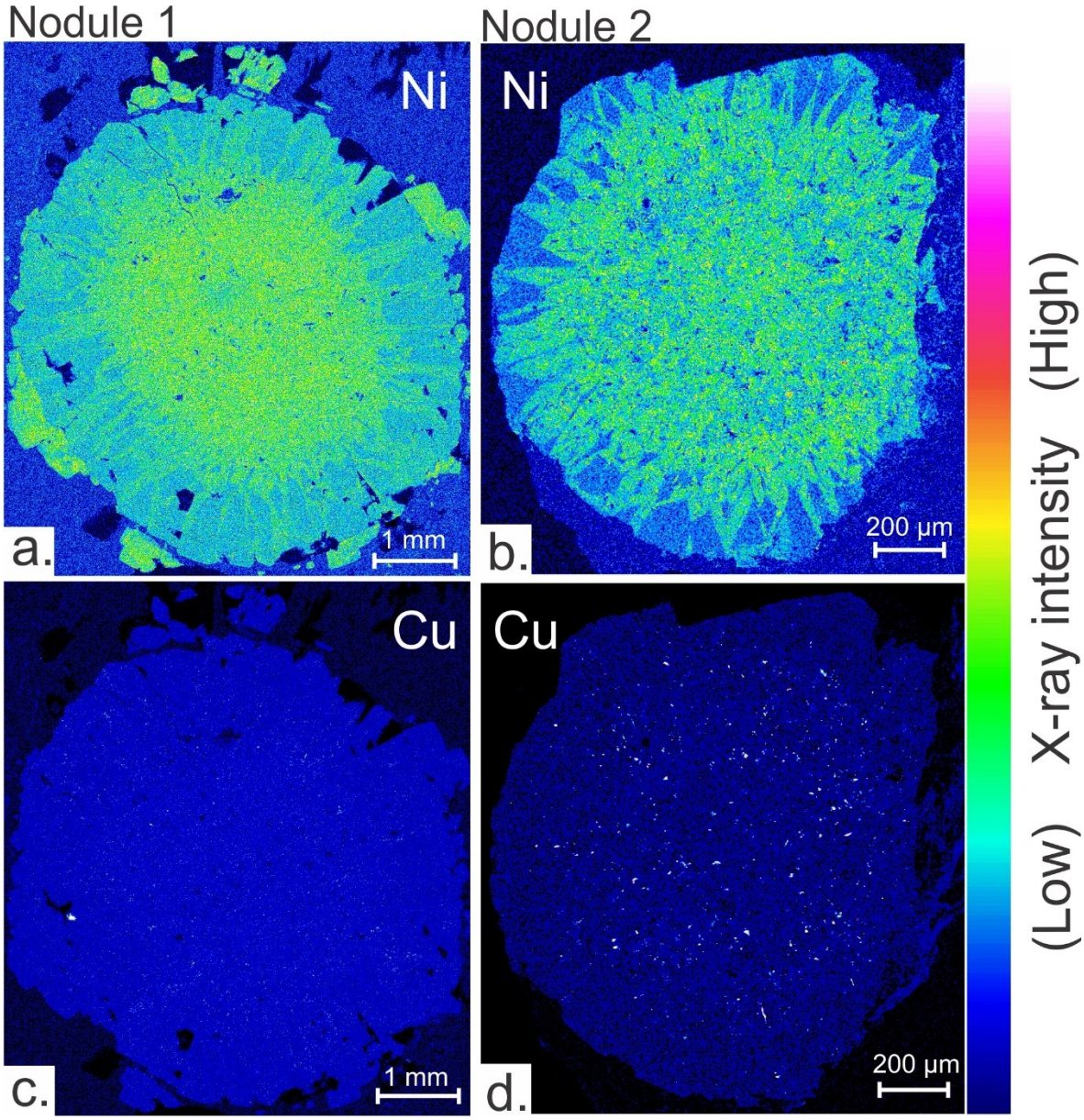

Figure 8. X-Ray elemental maps of Ni and Cu.

4.3. Multiple sulfur isotopes

The multiple sulfur isotopic data are listed in Table 2 and plotted in Figures 9-14. Overall, the isotopic values vary from -1.5 to 5.3‰ for $\delta^{34}S$, from -1.4 to 3.6‰ for $\Delta^{33}S$, and from -2.2 to 1.9‰ for $\Delta^{36}S$.

4.3.1. Pyrite nodules

Both pyrite nodule grains show similar sulfur isotopic ranges, e.g., $\delta^{34}S$ values from -1.4‰ to 2.4‰ for Nodule 1 and 1.2‰ to 2.7‰ for Nodule 2, $\Delta^{33}S$ values from -0.2‰ to 3.4‰ for Nodule 1 and -0.6‰ to 2.9‰ for Nodule 2, and $\Delta^{36}S$ value from -2.1‰ to 1.4‰ for Nodule 1 and -1.8‰ to 1.9‰ for Nodule 2 (Figures 9, 13, 14).

Similar to elemental distribution patterns, $\delta^{34}S$ and $\Delta^{33}S$ values of both nodules also show zonation patterns (Figures 9 & 13). The rims of pyrite nodules are characterized by relatively low $\delta^{34}S$ values (-1.4‰ to 0.8‰), relatively high $\Delta^{33}S$ values (2.1‰ to 3.4‰) and relatively low $\Delta^{36}S$ value (-2.1‰ to -0.5‰), whereas the cores of pyrite nodules display relatively high $\delta^{34}S$ values (-0.2‰ to 2.7‰) and relatively low $\Delta^{33}S$ values (-0.6‰ to 1.0‰), and relatively high $\Delta^{36}S$ value (0‰ to 1.9‰) (Figure 9, 10, 11).

4.3.2. Secondary subhedral pyrite disseminated in quartz veins/shadows

The secondary subhedral pyrite grains have relatively narrow isotopic ranges with $\delta^{34}S$ values from 3.5‰ to 5.3‰ (average: 4.6 ± 1.1‰; 2σ; n = 18), $\Delta^{33}S$ values from 0.4‰ to 1.3‰ (average: 0.8 ± 0.7‰; 2σ; n = 18), and $\Delta^{36}S$ values from -1.1‰ to 0.5‰ (average: -0.1 ± 0.8‰; 2σ; n = 18) (see Figures 12, 13, and 14).

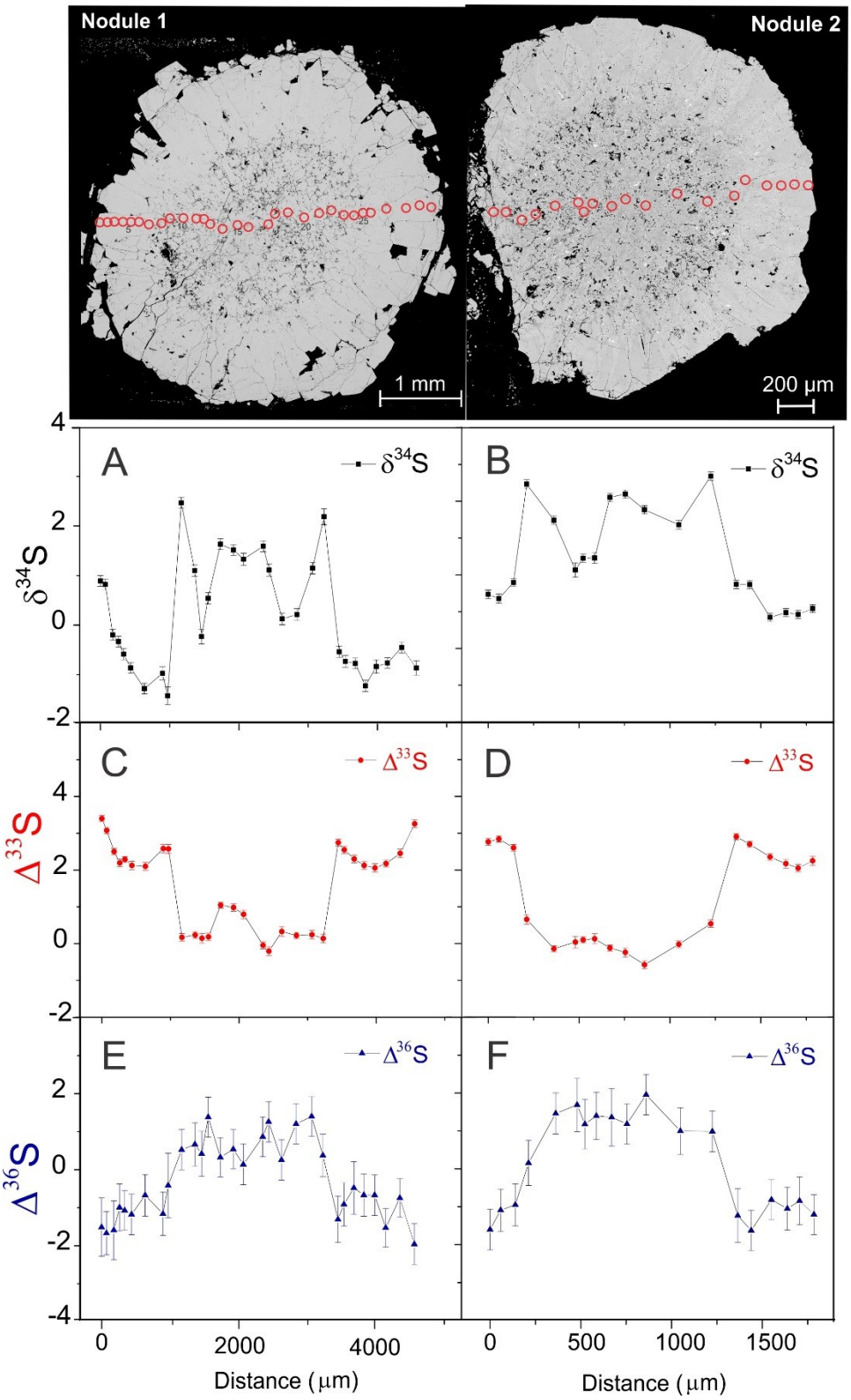

Figure 9. Variations of multiple sulfur isotope compositions of the two pyrite nodules. Red circles on the pyrite images mark the SIMS analytical positions.

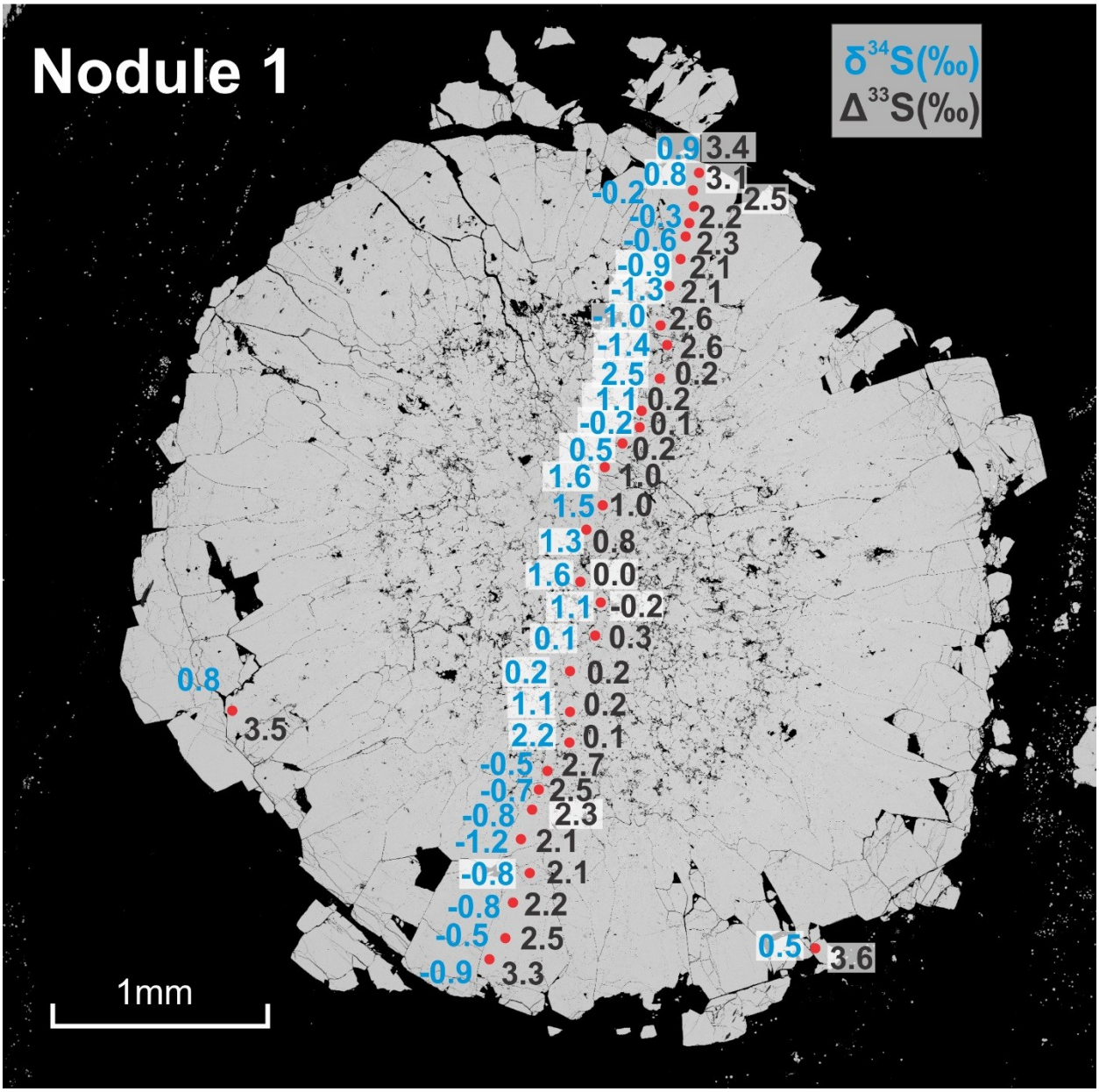

Figure 10. Cross-section variations of sulfur isotope compositions in Nodule 1. The analyzed spots are shown as red filled circles. The $\Delta^{33}S$ values are in black, and $\delta^{34}S$ values are in blue.

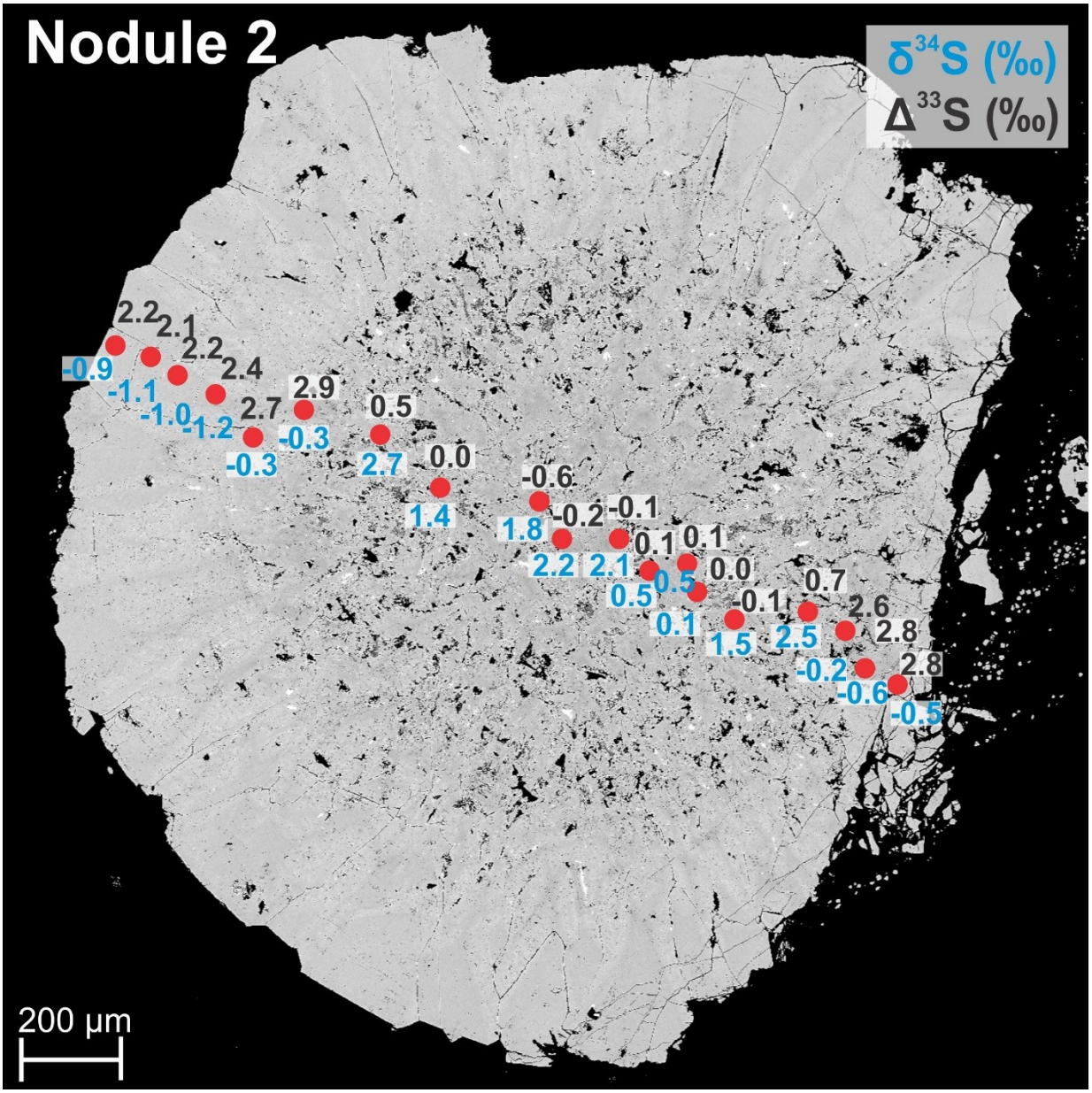

Figure 11. Cross-section variations of multiple sulfur isotope compositions in Nodule 2. The analyzed spots are shown as red filled circles. The $\Delta^{33}S$ values are in black, and $\delta^{34}S$ values are in blue.

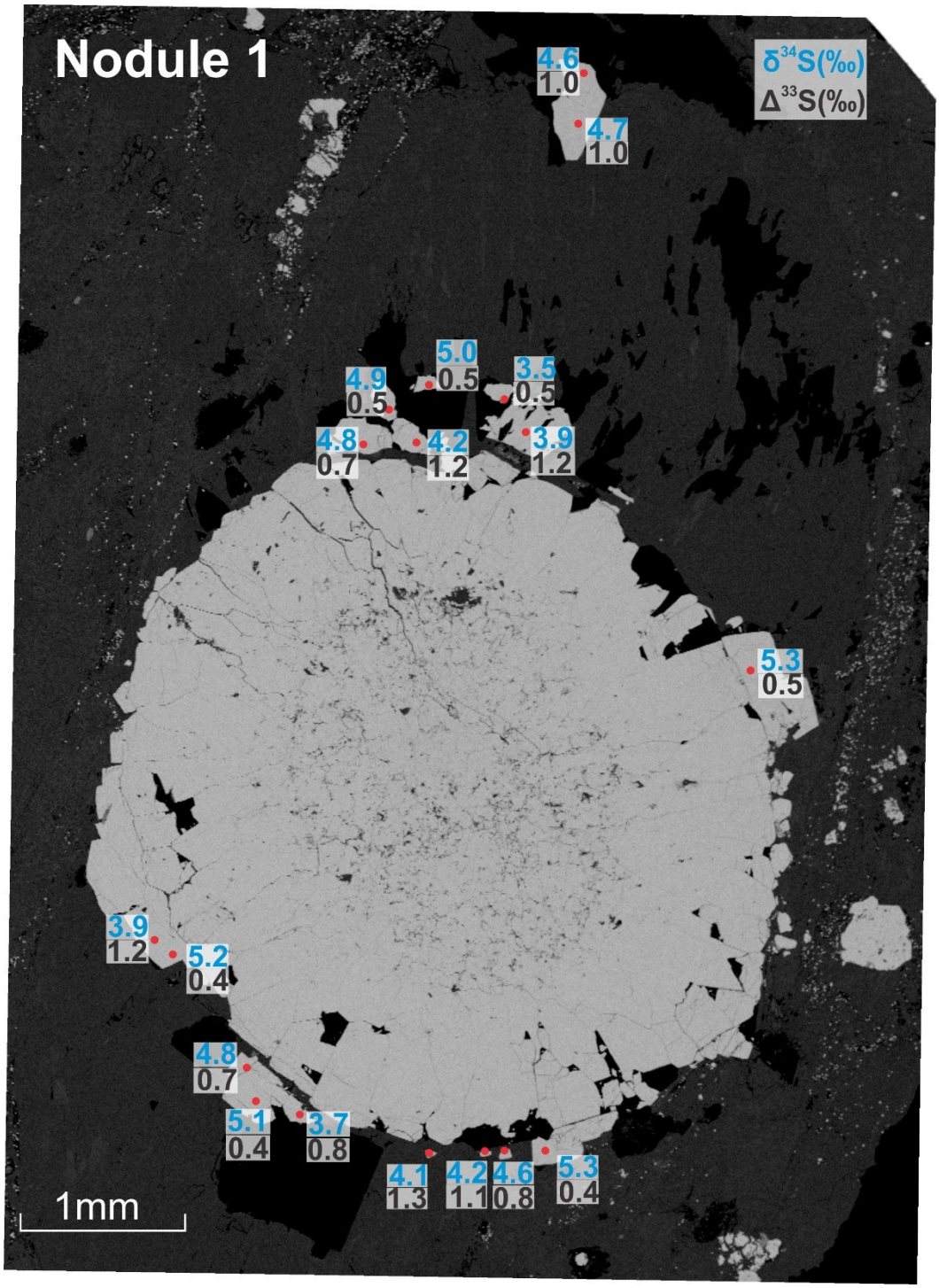

Figure 12. The multiple sulfur isotope compositions of secondary subhedral pyrites. The analyzed spots are shown as red filled circles. The $\Delta^{33}S$ values are in black, and $\delta^{34}S$ values are in blue.

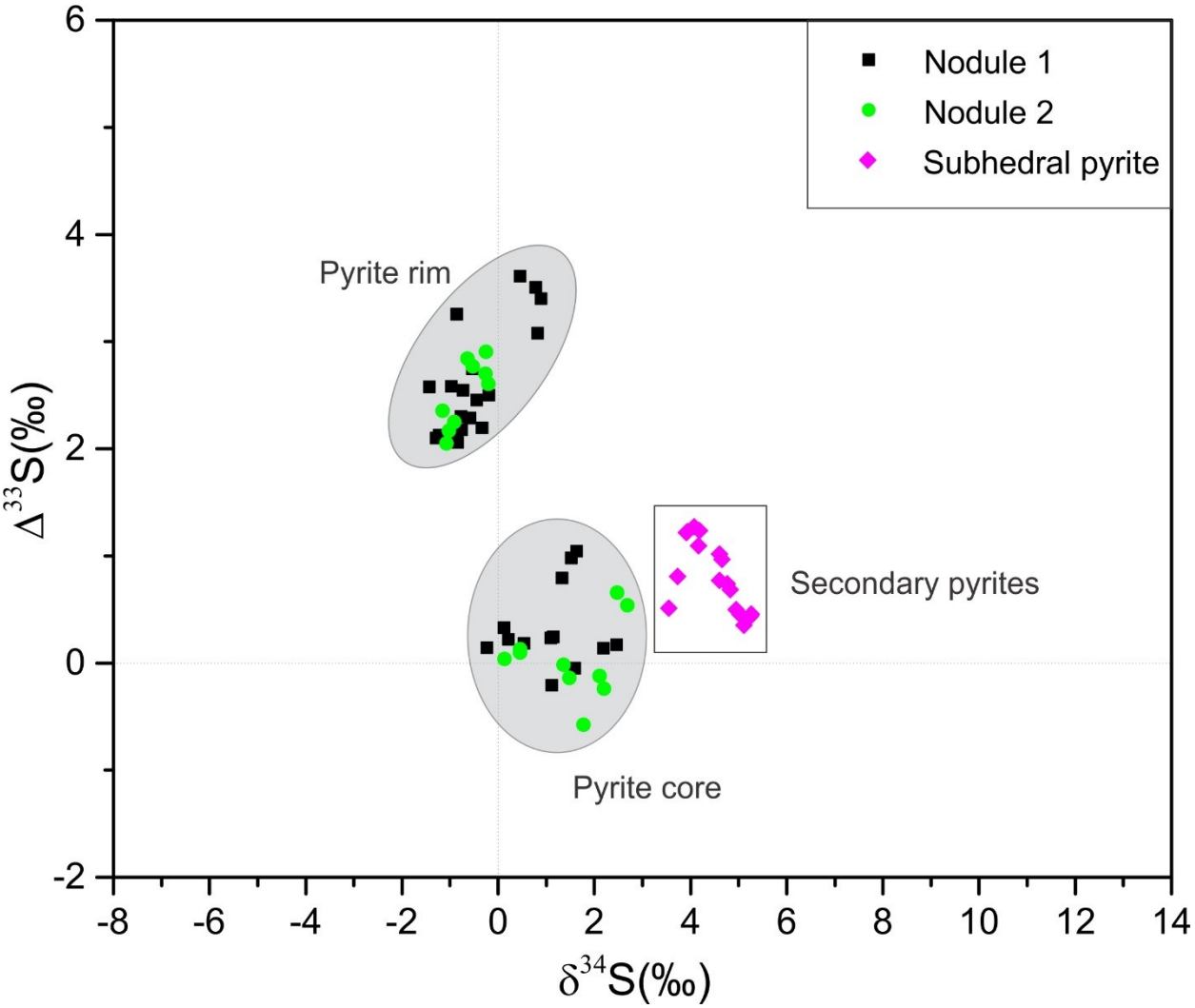

Figure 13. $\Delta^{33}S$ vs. $\delta^{34}S$ diagram comparing the sulfur isotopic data between the two pyrite nodules (in green and black, respectively) and secondary pyrite grains (magenta) in the Nimbus samples.

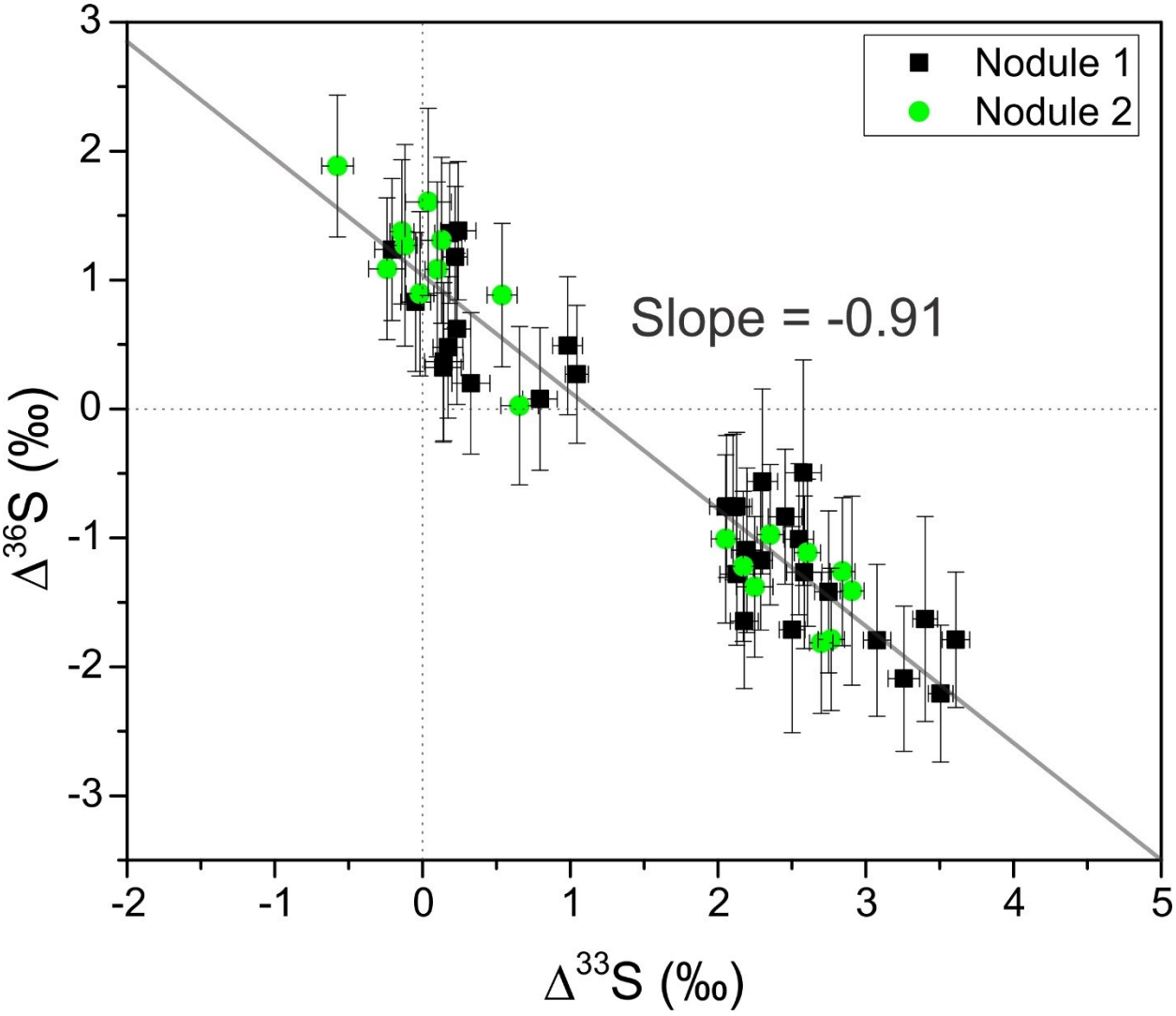

Figure 14. $\Delta^{36}S$ vs. $\Delta^{33}S$ diagram showing a good correlation with a slope of -0.9 for the two pyrite nodules (green and black) in the Nimbus samples.

5. Discussion

5.1. Diagenetic origin of pyrite nodules

Based on the petrographic evidence, we consider our pyrite nodules as authigenic pyrite rather than detrital pyrite from older rocks that have been weathered, transported and re-deposited. This conclusion is built on two lines of evidence.

Firstly, the studied pyrite nodules do not display typical detrital pyrite features. A good example of Archean detrital pyrite was found in the Witwatersrand basin in South Africa (Hofmann et al., 2009), where pyrites in a variety of morphologies including concretionary, compact rounded and idioblastic textures were consolidated (MacLean and Fleet, 1989). However, pyrites in this study show consistent rounded shape and zoning pattern with radiating-texture in rims which are suggested as a common feature for well preserved diagenetic pyrite (Rickard 2012, Steadman et al., 2015). Although detrital pyrites could also exhibit a rounded shape after long-distance transportation, those rounded detrital pyrites should show corroded rim pattern due to weathering and thus lose part of primary growth record as evidenced by truncated growth banding (MacLean and Fleet, 1989). However, the pyrite nodules from Nimbus conglomerates displayed a complete growth history without any abrasion features.

Secondly, although abundant detrital clasts exist in our samples, these clasts originated from igneous rocks (mainly dacites) and volcanic deposits (arkoses), which do not contain sulfide minerals except some scarce sub-micron sulfide grains formed during later hydrothermal alteration of the conglomerate. Few sulfide minerals observed within the altered clasts are fine-grained pyrite and sphalerite grains (Figure 4C & D), which were likely produced by hydrothermal alteration during metamorphism.

In addition, the multiple sulfur isotopic data show that the pyrite nodules bear significant S-MIF signal, which also rules out a magmatic origin of these sulfide minerals. Therefore, the pyrite nodules investigated in this study are regarded as authigenic rather than detrital pyrite.

5.2. Metamorphic effect on multiple sulfur isotopes

The Nimbus deposits have been subjected to hydrothermal alteration under lower greenschist-facies conditions, which is evidenced by the morphology and mineralogy described above. Therefore, it is necessary to assess the effect of metamorphism on the multiple sulfur isotope compositions of pyrite nodules before we can apply these data to discuss the Archean sulfur cycle.

Because the two selected pyrite nodule grains have not been fractured, the most likely altered parts of grains would be the rims. For this reason, whether the diagenetic pyrite nodules have been geochemically altered during metamorphism is mainly judged by comparing the elemental and isotopic signatures between the secondary subhedral pyrite grains in the pressure shadows and the rims of pyrite nodules. The elemental results show that the secondary pyrite grains contain high Ni concentration (0.07 ± 0.04%; Figure 15), different from the pyrite nodule rims that have undetectable Ni (Figure 15). Sulfur isotope data also show distinct features between secondary pyrite and diagenetic pyrite rim. The secondary pyrite grains have small variations in multiple sulfur isotope compositions characterized by high $\delta^{34}S$ (3.5‰ to 5.3‰) and low $\Delta^{33}S$ values (0.4‰ to 1.3‰), whereas the pyrite nodule rims have low $\delta^{34}S$ (-1.4‰ to 0.8‰) and high $\Delta^{33}S$ values (2.1‰ to 3.4‰) (Figures 13 & 15). The obvious differences in both elemental concentrations and sulfur isotope compositions indicate that the pyrite nodules have not been affected by the hydrothermal alteration and preserved their primary isotopic signature.

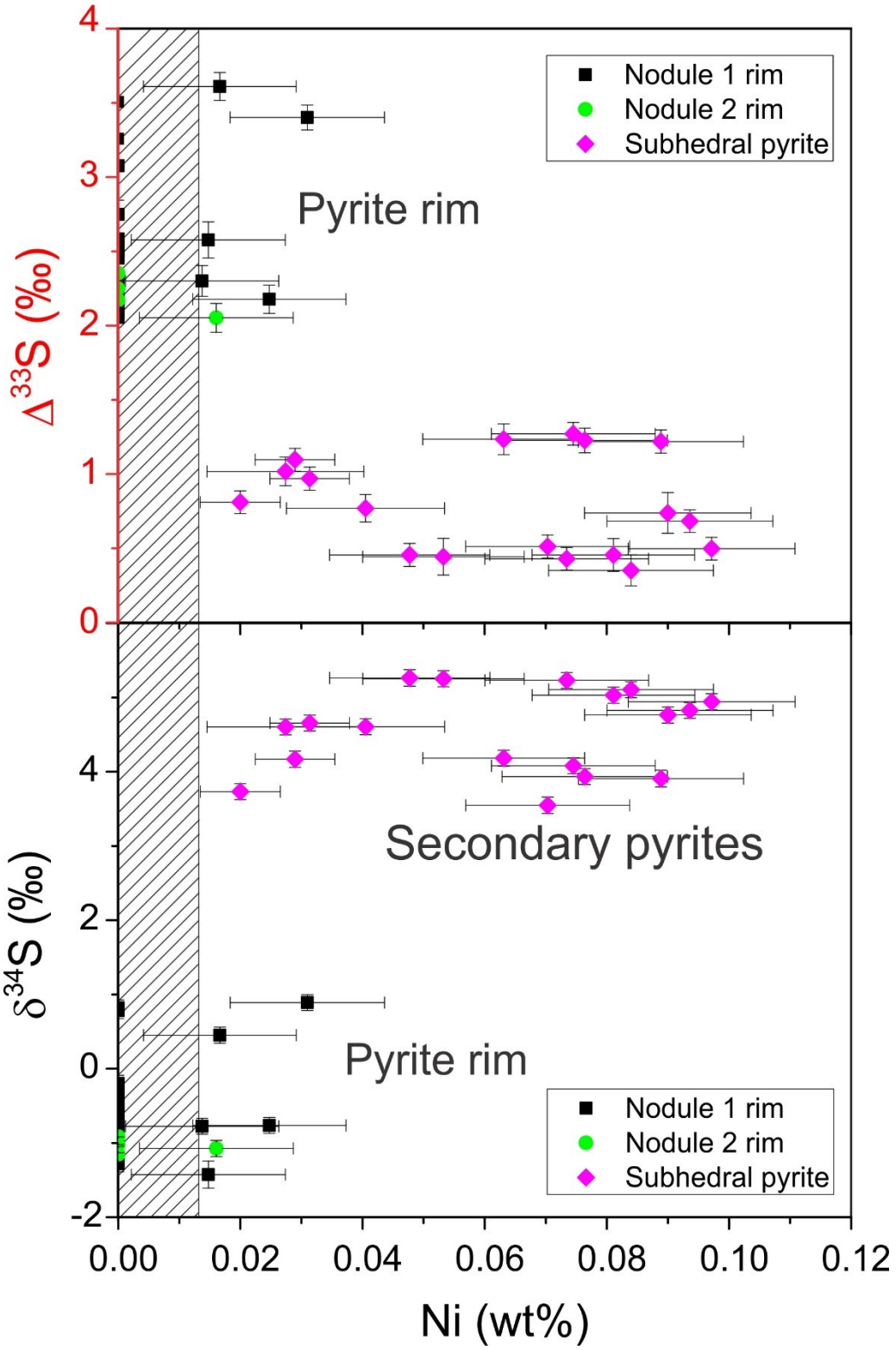

Figure 15. Comparison of multiple sulfur isotope compositions and Ni concentration between pyrite rims and secondary hydrothermal pyrite.

This is similar to our previous study on the 2.7 Ga pyrite nodules from the Joy Lake Sequence which also experienced lower greenschist-facies metamorphism (Li et al., 2017). Therefore, the nodules retain their primary sulfur isotope composition and can be used to infer the sulfur cycle when the sedimentary rock formed at 2.7 Ga.

5.3. Various sulfur sources for pyrite nodule growth

The studied pyrite nodules show striking isotopic zonation patterns. The cores have relatively low $\Delta^{33}S$ values (-0.6‰ to 1.0‰) and high $\delta^{34}S$ values (-0.2‰ to 2.7‰), whereas the rims show higher $\Delta^{33}S$ values (2.1‰ to 3.4‰) and lower $\delta^{34}S$ values (-1.4‰ to 0.8‰). The data on the pyrite cores do not show a clear trend on the $\Delta^{33}S$ vs. $\delta^{34}S$ diagram. However, the data for pyrite rims show a positive linear trend on the $\Delta^{33}S$ vs. $\delta^{34}S$ diagram (Figure 13).

Although the isotopic compositions of pyrite nodule cores are scattered, they all fall on or below the ARA (Figure 16). Whereas $\Delta^{33}S$ show both negative and positive values, all $\delta^{34}S$ values except one are higher than 0‰. These data define mixing between three end-members: Archean seawater sulfate ($\delta^{34}S \approx 4.5$‰, $\Delta^{33}S \approx -1.5$‰; E1 in Figure 16), submarine volcanic or hydrothermal sulfide ($\delta^{34}S = 0$‰, $\Delta^{33}S = 0$‰; E2 in Figure 16) and elemental sulfur from ARA ($\delta^{34}S \approx 7$‰, $\Delta^{33}S \approx 8$‰; E3 in Figure 16), among which the submarine volcanic/hydrothermal endmember was dominant.

Between the core and the inner rim area of pyrite nodules, the isotopic data show an abrupt increase for 2.6‰ in $\Delta^{33}S$ value and a decrease for 1.1‰ in $\delta^{34}S$ value (Figure 9). This change is strikingly shown in Figure 17, in which the distance of each analytical spot from the core was normalized to the distance from the core to the rim. Such abrupt isotopic shifts from the core to the inner rim imply a fundamental change in pyrite formation environment that resulted in a change of sulfur source and/or a change in microbial metabolic pathway (see detailed

discussion below). The positive $\Delta^{33}S$ values from the inner rim area indicate a significant contribution of atmospheric elemental sulfur, but their negative $\delta^{34}S$ values suggest the elemental sulfur source was not directly from ARA.

There are two possible explanations for a sulfur pool with a positive $\Delta^{33}S$ value but a negative $\delta^{34}S$ value. The first is a sulfide pool derived from the bacterial reduction of the elemental sulfur of ARA. The elemental sulfur of ARA is commonly observed in Archean sulfide records and is characterized by positive $\Delta^{33}S$ (5‰ – 8‰) and positive $\delta^{34}S$ value (6‰ – 10‰) (Ono et al., 2003) (e.g., E3 in Figure 16). If a small fraction of such elemental sulfur is reduced, the associated MDF can induce the sulfide product to be ^{34}S-depleted while maintaining its original $\Delta^{33}S$ signature. The bacterial reduction of elemental sulfur can be processed in two ways: (1) dissimilatory reduction of elemental sulfur, which is characterized by very small $^{34}S/^{32}S$ fractionation with $\delta^{34}S$ values of sulfide up to ~5‰ lower than the initial value of elemental sulfur (Surkov et al., 2012). This isotopic shift magnitude cannot reach the observed negative $\delta^{34}S$ values in our study; (2) disproportionation of elemental sulfur, which can produce sulfide with $\delta^{34}S$ values from 3.7‰ to 11.0‰ and sulfate with $\delta^{34}S$ values up to 34‰ higher than elemental sulfur (Canfield and Thamdrup, 1994; Canfield et al., 1998; Böttcher et al., 2001). Repeated steps of sulfide oxidation coupled with elemental sulfur/sulfite disproportionation can result in a total effect on $\delta^{34}S$ of up to 70‰ lower in sulfide (Johnston et al., 2005b). In geological records, elemental sulfur disproportionation (ESD) is generally reflected by large isotopic fractionation, which is not observed in this study, and most commonly seen in the Proterozoic geological records (Canfield and Teske, 1996; Johnston et al., 2005b). Another difficulty in using elemental sulfur disproportionation to explain the rim isotopic data is that a significant sulfate reservoir with very high $\delta^{34}S$ and similar $\Delta^{33}S$ values simultaneously produced

by ESD has to be ignored. In addition, ESD can only produce $\Delta^{33}S$ up to 0.1‰ (Johnston et al., 2005b), which is not consistent with the large $\Delta^{33}S$ variation (1.3‰) in the rims as observed in Nimbus samples.

The second and more straightforward explanation for a sulfur pool with a positive $\Delta^{33}S$ value but negative $\delta^{34}S$ value is elemental sulfur derived directly from the FVA (Philippot et al., 2012; Muller et al., 2016). Our data deviate slightly to the right of FVA by around 2‰ in $\delta^{34}S$ (Figure 17). This can be explained by the existence of a small amount of background elemental sulfur from the ARA (see discussion below).

The potential occurrence of FVA-type elemental sulfur in our study area is consistent with its geological setting as a back-arc or rift (Barley et al., 1989; Krapez, 1997; Czarnota et al., 2010; Hollis et al., 2017). Besides major sub-aerial volcanic eruptions occurring in the arc, some major volcanic eruptions can also occur in rifting setting. A good example is Iceland, where many volcanic eruptions have been observed and documented. In particular, the Laki eruption in 1783, one of the largest volcanic eruptions in decades (Þórðarson and Self, 2001), generated a sulfuric aerosol haze covering a large part of the Northern Hemisphere for approximately eight months. Both arc- and rift-related eruptions may send huge amounts of SO_2 into the atmosphere (Andres and Kasgnoc, 1998). For example, the SO_2 emission in modern African Rift is estimated at about 1.6-2.1 $\times 10^{12}$ g/yr, which is close to those in modern arc system such as Japan (1.9-2.7$\times 10^{12}$ g/yr) (Halmer et al., 2002). An abrupt increase in volcanic SO_2 in the atmosphere could have changed the photochemical effects on the elemental sulfur product and subsequently produced different $\delta^{34}S$ and $\Delta^{33}S$.

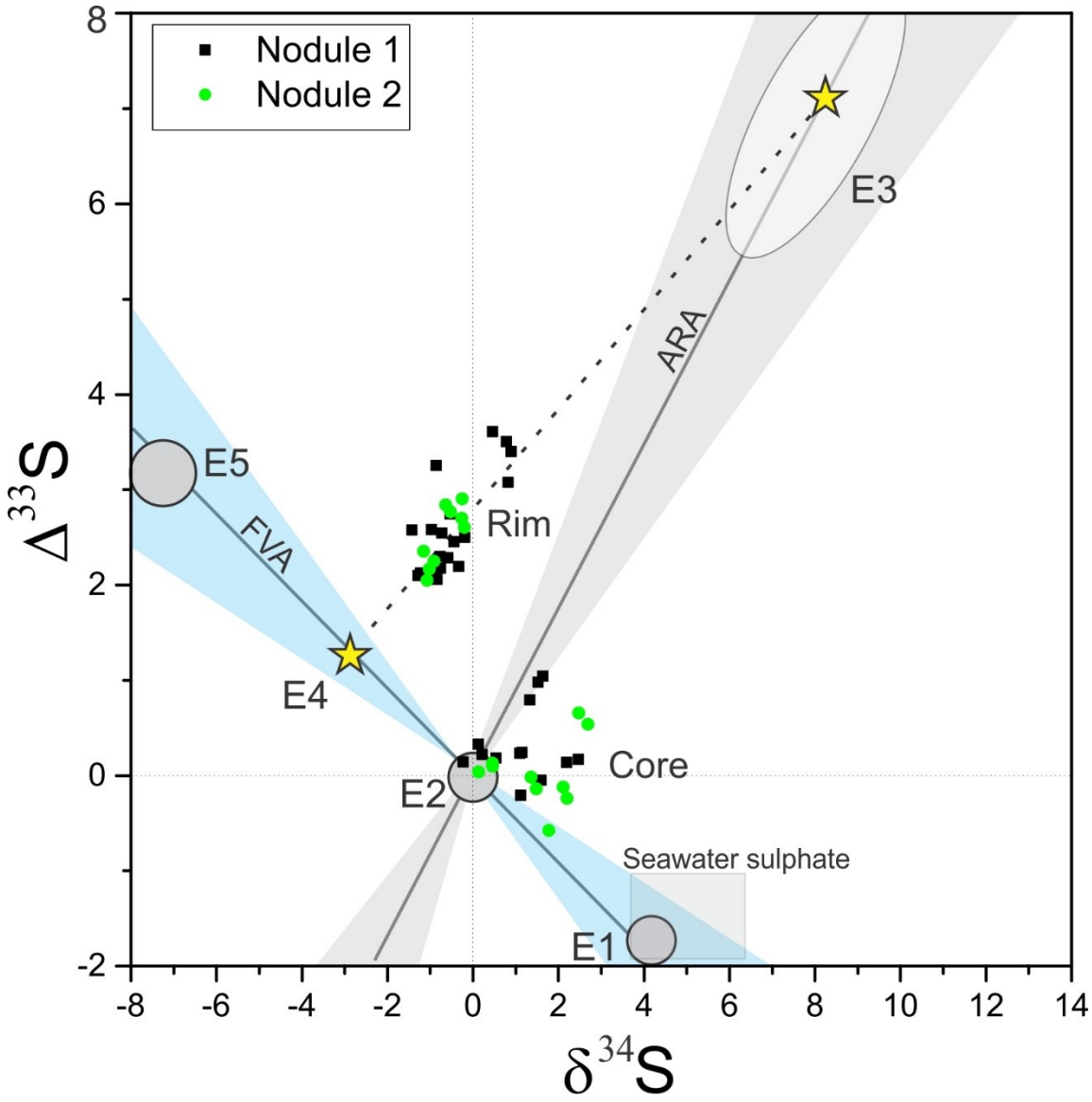

Figure 16. $\Delta^{33}S$-$\delta^{34}S$ diagram showing the sulfur isotope compositions of Nimbus pyrite nodules and their potential sulfur sources. The grey ellipse represents ARA-type elemental sulfur in Ono's model (Ono et al., 2003). The filled square represents seawater sulfate (Chen et al., 2015). The yellow stars represent two endmembers of sulfur source accounting for the rims of the pyrite nodules. The grey circles represent other potential sulfur sources for pyrite nodules (see text for discussion).

From the inner rim to outer rim areas of the two pyrite nodules, the $\delta^{34}S$ and $\Delta^{33}S$ values first decrease from -0.2‰ to -1.4‰ and 2.6‰ to 2.1‰ respectively (Stage 2 in Figure 17), and then increase from -1.4‰ to 0.9‰ and 2.1‰ to 3.6‰ (Stage 3 in Figure 17). Overall, the data from the pyrite nodule rims show a linear correlation between $\delta^{34}S$ and $\Delta^{33}S$ with a slope of 0.54 (R^2=0.78) (Figure 16). Since we have already excluded the metamorphic effect, and most S-MDF processes will not influence the $\Delta^{33}S$ values (Johnston et al., 2005a; Johnston, 2007), this isotopic shift from the inner to outer rim areas may be explained by two possible scenarios as detailed below.

The first is thermochemical sulfate reduction (TSR). Since the pyrite was formed in the tectonically active environment, hydrothermal fluids supplied to the environment could promote TSR and consequently increase the $\Delta^{33}S$, as observed by Watanabe et al. (2009) in their experiments. However, TSR can only shift the $\Delta^{33}S$ values but have little effect on $\Delta^{36}S$ values (Oduro et al., 2011). Our results show a good correlation between $\Delta^{33}S$ and $\Delta^{36}S$ values (Figure 14), and thus rule out this possibility.

The second and more likely explanation for this linear relationship is a two end-member mixing. A linear fitting of the rim data gave a lower interception on the FVA with $\delta^{34}S$ = -2.9‰ and $\Delta^{33}S$ = 1.2‰ (E4 in Figure 16) and an upper interception on the ARA at $\delta^{34}S$ = 8.2‰ and $\Delta^{33}S$ = 7.2‰ (E3 in Figure 16). The upper intercept fits well with the elemental sulfur reservoir in the ARA model by Ono et al. (2003). The lower interception could be either a pure FVA-like elemental sulfur (E4 in Figure 16), or a mixture from (1) seawater sulfate (E1 in Figure 16), (2) submarine volcanic/hydrothermal sulfur (E2 in Figure 16; Peters et al., 2010), and (3) FVA-like elemental sulfur with more depleted $\delta^{34}S$ (e.g., E5 in Figure 16). So far, there is no efficient tool to distinguish between these two possibilities.

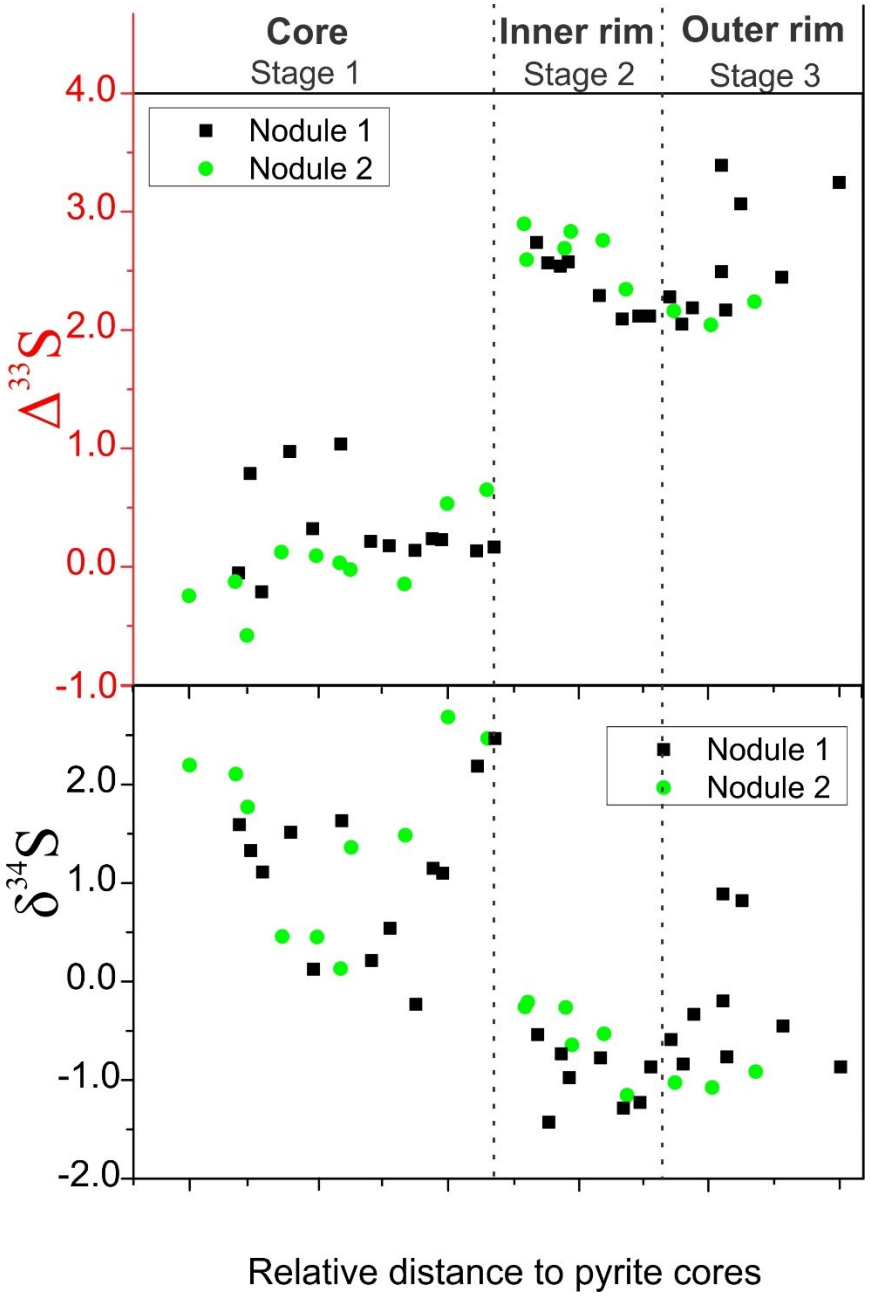

Figure 17. Multiple sulfur isotopic variation from cores to rims in pyrite nodules. The relative distance refers to the actual distance of each point normalized to the distance between the core and rim.

In the inner rim areas of the pyrite nodules, both $\Delta^{33}S$ and $\delta^{34}S$ values steadily decrease from 2.6‰ to 2.1‰ and -0.2‰ to -1.4‰, respectively (Stage 2 in Figure 17). Following above interpretation, this trend may indicate an enhanced contribution of FVA-type elemental sulfur during this growth period. In the outer rim areas of the pyrite nodules, $\Delta^{33}S$ and $\delta^{34}S$ values steadily increase from 2.1‰ to 3.6‰ and from -1.4‰ to 0.9‰, respectively (Stage 3 in Figure 17). This co-variation may indicate that, by the time of the growth of this rim part, the contribution of the FVA-like elemental sulfur started to decrease, probably due to the diminished volcanic activities, and the background ARA-like elemental sulfur became more significant in the system. Li et al. (2017) speculated that the volcanic eruptions generally lasted for a relatively short time period and could only modify the atmospheric chemistry at the local scale. Following the decrease in volcanic SO_2 emission, the atmospheric chemistry could recover quickly to the normal background level as a result of rigorous atmospheric circulation. This change would gradually switch the sulfur isotopic compositions of elemental sulfur from the FVA-like to the ARA-like signature.

In summary, we consider the FVA-like elemental sulfur (although short-lived) as an important sulfur source for pyrite formation, because (1) it can better explain the multiple sulfur isotope compositions recorded in the pyrite nodules, and (2) it is consistent with the geological settting of the deposit.

5.4. Environmental and formation mechanisms for pyrite nodule

Strong isotopic heterogeneity has been observed in pyrite grains. For example, in modern sediments, the pyrite from coastal California shows large $\delta^{34}S$ variation from -35‰ to -18‰ from core to rim (Kohn et al., 1998). In addition, Kozdon et al. (2010) have reported a $\delta^{34}S$ variation from -2 to +6‰ over 10 mm within a pyrite grain collected from the ~3.5 Ga cherts in the Pilbara Craton, Western Australia. Furthermore, a co-variation of iron and sulfur isotopes has been observed in the sedimentary pyrite from the 2.7 Ga Belingwe Greenstone belt, Zimbabwe (Archer and Vance, 2006). These isotopic variations have been mainly explained by progressive ^{34}S enrichment as a result of the Rayleigh distillation effects in a closed system.

The precise measurement of multiple sulfur isotope compositions provide a robust tool to re-evaluate the formation environment and mechanism of large sulfide grains, because complementary indices of $\Delta^{33}S$ and $\delta^{34}S$ can shed insights into both sulfur sources and biogeochemical processes. With the development of high-resolution *in-situ* analytical method (e.g., SIMS), large $\Delta^{33}S$ variation has been reported in single pyrite grains over micro-scales (e.g., Kamber and Whitehouse, 2007; Williford et al., 2011; Farquhar, 2013; Fisher et al., 2014; Marin-Carbonne et al., 2014; Gregory, 2015; Steadman et al., 2015; Li et al., 2017). For example, Marin-Carbonne et al. (2014) have reported increasing $\Delta^{33}S$ (from -1.6 to +2.9‰) and $\delta^{34}S$ (from -0.5 to +8.2‰) from the core to the rim in sedimentary pyrite nodule from the ~2.7 Ga shale in the Bubi Greenstone Belt, Zimbabwe. Similarly, a pyrite nodule from the ~2.5 Ga Mount McRae Formation, South Africa shows $\delta^{34}S$ values around 0.5‰ and $\Delta^{33}S$ values around 1.2‰ in the core to $\delta^{34}S$ around 9.6‰ and $\Delta^{33}S$ around 7.3‰ in the rim (Williford et al., 2016). In addition, Li et al. (2017) reported a negative correlation between $\Delta^{33}S$ and $\delta^{34}S$ values, with the $\Delta^{33}S$ values from -2.9‰ to +0.3‰ and $\delta^{34}S$ values from +2.0‰ to -2.9‰ from the cores to the rims in pyrite nodules. It is worth noting that not all Archean pyrite nodules have displayed

large heterogeneity as discussed above. For example, pyrite nodules from the ~2.7 Ga Tumbiana Formation have nearly constant $\Delta^{33}S$ (around 0.3~0.9‰) and variable $\delta^{34}S$ from -8‰ to 0.4‰ (Williford et al., 2016). Nevertheless, these varying $\Delta^{33}S$ and $\delta^{34}S$ values on single pyrite grains from the Archean sediments indicate a complex formation mechanism involving various sulfur sources (e.g., atmospheric-derived elemental sulfur, seawater sulfate) and different microbial activities during diagenesis rather than a simple Rayleigh distillation effect in a closed system.

To better explain the intra- and inter-grain sulfur isotopic heterogeneity, two distinct pathways have been proposed for pyrite formation (Farquhar et al., 2013): (I) sulfide pathway, and (II) polysulfide pathway, which can be described as below:

I. Sulfide pathway: $FeS_m + H_2S \rightarrow FeS_2 + H_2$ (1)

II. Polysulfide pathway: $FeS_m + S_{n+1}^{2-} \rightarrow FeS_2 + S_n^{2-}$ (2)

in which "m" means mackinawite, and "n" means variable numbers of sulfur atoms.

In the sulfide pathway, the mackinawite (FeS_m) would react with H_2S to produce pyrite and hydrogen gas. The isotopic composition of pyrite formed through this pathway is 1:1 mixing between FeS_m and H_2S (Butler et al., 2004).

In the polysulfide pathway, the FeS_m reacts with polysulfide (S_{n+1}^{2-}) to produce pyrite and polysulfide (S_n^{2-}). The reactant polysulfide is considered to be mainly derived from elemental sulfur by reaction between elemental sulfur and HS^-:

$$n/8\ S_8 + HS^- \rightarrow S_{n+1}^{2-} + H^+ \quad (3)$$

As a result, the isotopic signature of polysulfide mainly inherits the isotopic signature of elemental sulfur (Butler et al., 2004).

These two pathways can occur con? but compete with each other depending on relative availability of H_2S and elemental sulfur (S_8) (Rickard, 2012). If the S_8 concentration is low and

H_2S dominates in the system, pyrite would be mainly formed through the sulfide pathway, and thus record a mixed sulfur isotopic signature. If S_8 is more abundant than sulfide in the system, pyrite would be mainly formed through the polysulfide pathway and thus bear isotopic signature close to elemental sulfur (Rickard, 2012). Thus, a positive $\Delta^{33}S$ shift from pyrite cores to rims is more likely due to progressive enrichment of elemental sulfur or depletion of sulfide in the porewater, which can eventually shift the pyrite formation mechanism from sulfide pathway to polysulfide pathway.

The multiple sulfur isotope compositions of the pyrite nodules studied here suggest a complicated growth history under a changing environment and sulfur source. The pyrite nodules display a rounded shape, which suggests continuous growth in a high degree of supersaturation condition (Rickard, 2012). The combined $\Delta^{33}S$ and $\delta^{34}S$ data rule out the possibility of a Rayleigh distillation effect in a closed system, which has been proposed as a favorable formation environment for pyrite nodule growth based solely on the $\delta^{34}S$ data. The trace element (Cu and Ni) data, showing relatively higher values in the core but below detection limit levels in the rim, do not either fit with a Rayleigh distillation model. These data suggest at least a semi-closed or even an open system with sufficient external sulfur supply during the growth of the pyrite nodules.

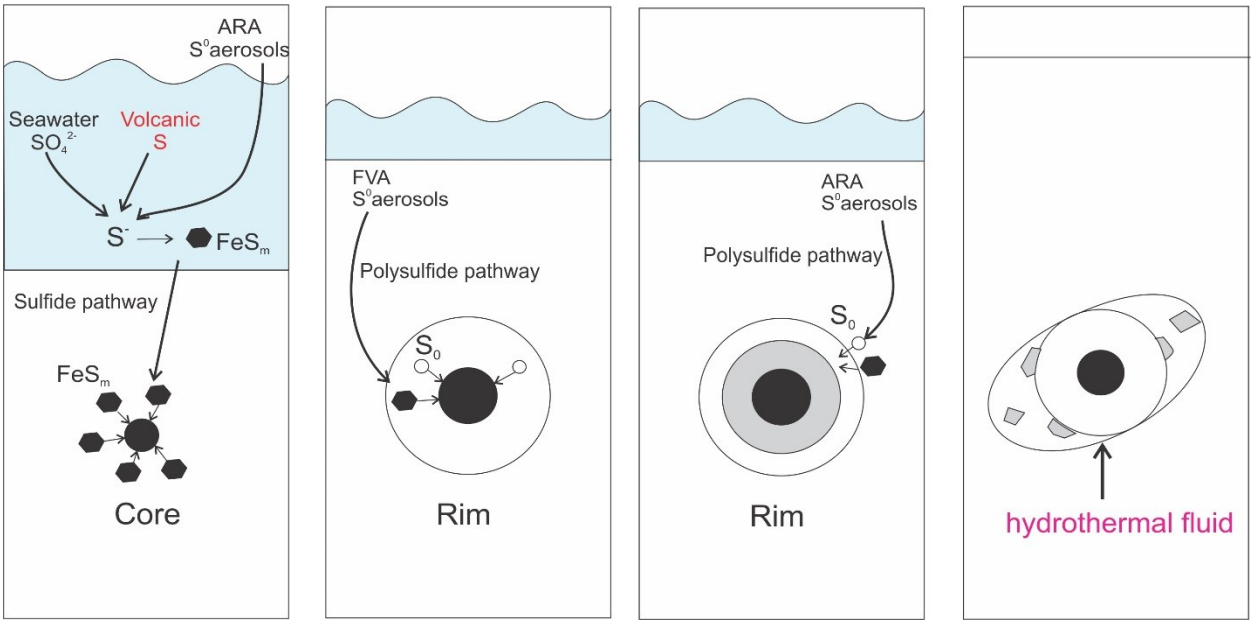

Figure 18. Schematic cartoons showing formation and metamorphic history of the pyrite nodules in the Nimbus deposits.

A schematic 4-stage growth model for pyrite nodules in this study is shown in Figure 18. In Stage 1, the core of pyrite nodules forms with variable sulfur contributions from seawater sulfate, ARA-type elemental sulfur, and submarine volcanic sulfur. The pyrite core is likely formed through a sulfide pathway. Stage 2 is initiated by strong volcanic activity. Sub-aerial volcanism ejects abundant sulfur aerosols into the stratosphere in a short time, which subsequently introduces abundant elemental sulfur into ocean and porewater (ten times higher than normal level) (Mishima, 2017). Since the Archean seawater is characterized by a very low sulfate level (Canfield et al., 2000; Habicht et al., 2002; Jamieson et al., 2013; Crowe et al., 2014), the down wash of FVA-type elemental sulfur could significantly change the local concentration and isotopic signature of the porewater sulfur pool, whereas the co-produced sulfate with a similar isotopic compositions to the seawater sulfate (Muller et al., 2016) could be quickly diluted by seawater circulation and thus not affect the local sulfate pool significantly.

The elevated elemental sulfur concentration in the system could subsequently shift the pyrite formation mechanism from the sulfide pathway to the polysulfide pathway. In Stage 3, while volcanic activity diminishes, the supply of FVA-like elemental sulfur decreases quickly and the total elemental sulfur poor in the porewater system consequently shifts from the FVA-like to the background ARA-like elemental sulfur, which results in a steady increase in $\Delta^{33}S$ and $\delta^{34}S$ values at the outer rim (Figure 16). In Stage 4, late metamorphic fluids further precipitate the subhedral pyrite in the pressure shadows but not affect the geochemical characteristics of pyrite nodules.

5.5. An oscillating environment at the margin of Kalgoorlie and Kurnaple Terranes at 2.7 Ga.

Following the first FVA-like signal reported from the 2.7 Ga Joy Lake sequence in the Superior Province (Minnesota, USA), here we report another multiple sulfur isotope record showing the volcanic effect on the 2.7 Ga sulfur cycle from the Nimbus deposits in the Kalgoorlie Terrane, Western Australia. This implies that volcanic effect on Archean sulfur cycle may not be a rare phenomenon. While the multiple sulfur isotopic data available for the Superior Province are very few, more data are available in the vicinity of the Nimbus deposit and surrounding area, which provides a good opportunity to assess the volcanic effect on a regional scale.

The sedimentary pyrite nodules from the Paringa interflow shale and the Kapai Slate in the Golden Mile deposits could be another case to reflect the volcanic effect. The Golden Mile deposits are only 17 km northwest of Nimbus deposits (Figure 19A). The Paringa interflow shale and the Kapai Slate also form part of the Kambalda Sequence at the margin of the Kurnalpi Terrane (Figure 19B; Swager and Griffin, 1990). The age of the Paringa interflow shale is

constrained to be 2689-2688 Ma, and the age of Kapai Slate is about 2692 ± 4 Ma (Claoué-Long et al., 1988). Steadman et al. (2015) reported multiple sulfur isotope compositions of three pyrite nodules from this area. One pyrite nodule from the Paringa interflow (I in Figure 19C) shows very large isotopic heterogeneity with low $\Delta^{33}S$ value (around -2‰) and a high $\delta^{34}S$ value (~ 4‰) close to the seawater sulfate endmember in the core, and a very high $\Delta^{33}S$ value (up to 5‰) and a near-zero $\delta^{34}S$ value in the rim. This pattern is very similar to that in the Nimbus pyrite nodules. The second pyrite nodule from the Paringa interflow (II in Figure 19C) shares a similar sulfur isotopic signature, although the $\Delta^{33}S$ range is much smaller and $\Delta^{33}S$/ $\delta^{34}S$ slope is gentler. The third pyrite nodule, which is from the Kapai Slate, shows similar isotopic ranges but more scattered values in $\Delta^{33}S$ and $\delta^{34}S$ (III in Figure 19C) compared with pyrite nodules from the Paringa interflow and the Nimbus pyrite nodules. The Kapai Slate pyrite nodule has a positive-slope linear correlation between $\Delta^{33}S$ and $\delta^{34}S$ from core to the middle part, which is slightly shifted toward the FVA endmember at the rim. It is possible that ARA was dominating during most of the time period of the nodule formation, and the FVA was added at the final stage.

Chen et al. (2015) studied the multiple sulfur isotope data of some samples from the Jaguar VHMS deposits of the Yilgarn Craton, West Australia. The Jaguar deposit is located about 300 km north of the Nimbus mine in the west margin of the paleo-rifting Kurnaple Terrain as part of the Teutonic Bore volcanic complex (Figure 19A). The depositional age of the Jaguar deposits is estimated as 2.692 Ga (Greig, 1984; Brown et al., 2002), which is close to that of the Nimbus and the Golden Mile deposits. Among various types of pyrites in the Jaguar VHMS deposits, some large pyrite patches exhibit core – rim zonation similar to pyrite nodules. High-resolution analysis of one of such pyrite patch shows $\delta^{34}S$ values of around 0‰ to 2 ‰ and $\Delta^{33}S$

values of around 0‰ to 1‰ (IV in Figure 19C; Chen et al., 2015) with a distribution pattern similar to the pyrite nodules in this study.

In summary, the pyrite nodules from Nimbus, Golden Mile, and Teutonic Bore extended along an N-S direction for more than 300 km, all share common sulfur isotopic features, not only in the ranges of $\Delta^{33}S$ and $\delta^{34}S$ values, but more importantly a negative-slope linear trend between $\Delta^{33}S$ and $\delta^{34}S$ values (Figure 19). If this trend was indeed caused by addition of elemental sulfur produced by special photochemical reactions related to intensive volcanic SO_2 input as we propose here, the widespread distribution of such trend suggests that the volcanic effect on the atmospheric sulfur cycle in 2.7 Ga could be much more significant than previously thought.

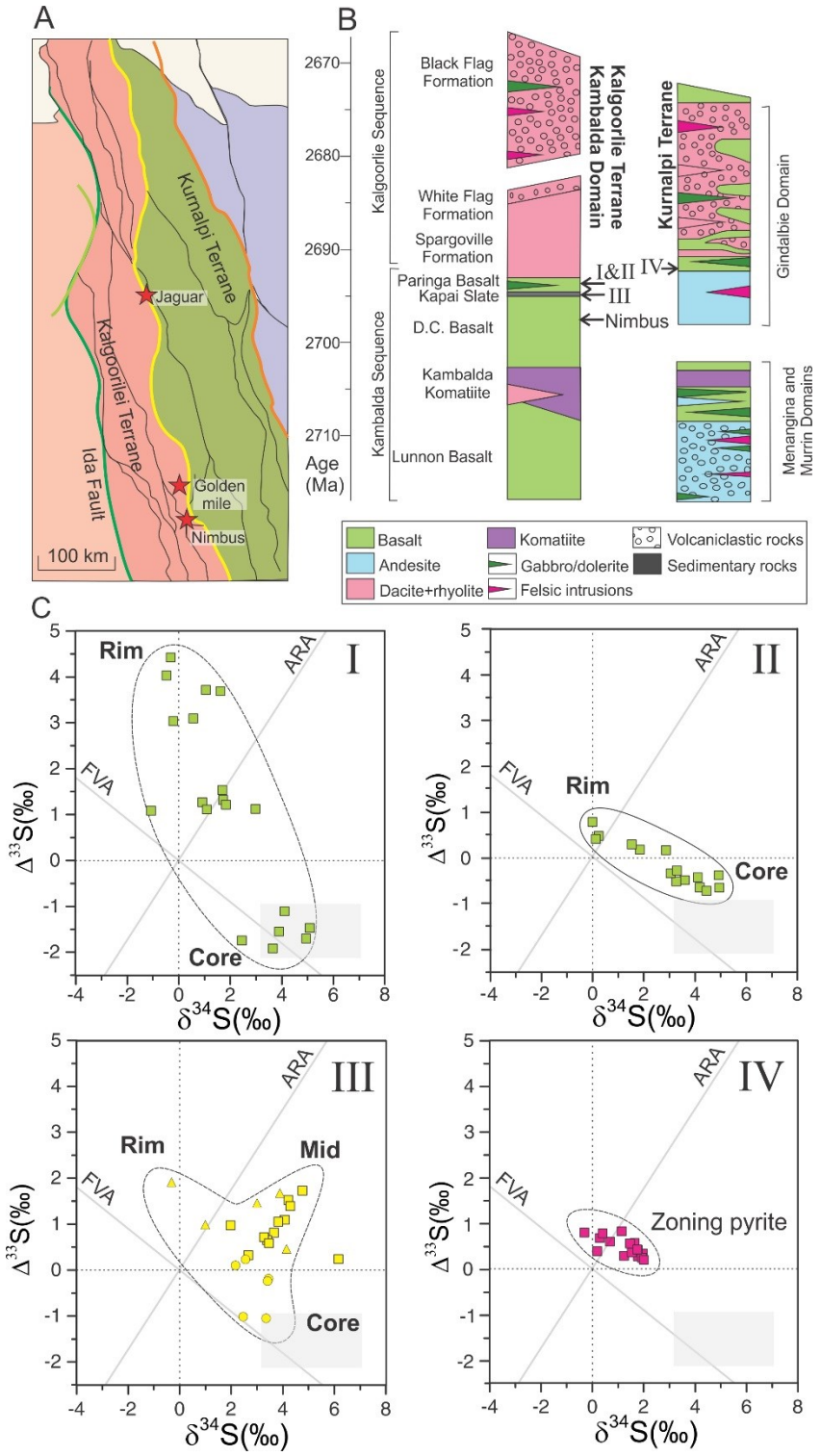

Figure 19. A. a location map of the Yilgarn Craton (After Cassidy et al., 2006). The red-filled stars show the location of analyzed samples for multiple sulfur isotopes. B. the regional stratigraphy of Kalgoorlie and Kurnalpi Terranes (after Barnes and Van Kranendonk, 2014) C. $\Delta^{33}S$ - $\delta^{34}S$ plots of sedimentary pyrites of the 2.7 Ga Eastern Goldfields Superterrane of Yilgarn Craton, data collected from (Chen et al., 2015; Steadman et al., 2015).

6. Conclusion

In order to test the volcanic effect on the sulfur cycle in 2.7 Ga, we studied the sedimentary pyrite nodules from the 2.7 Ga Nimbus VHMS deposits in the Kalgoorlie Terrane within the Eastern Goldfields Superterrane, West Australia.

We first compared the isotopic signatures between the large diagenetic pyrite nodules and small secondary subhedral pyrite grains in quartz veins that were deposited from the metamorphic fluid. The results show that the diagenetic pyrite nodules have very different multiple sulfur isotope compositions to the secondary pyrite grains, suggesting that the primary isotopic signature of the diagenetic pyrite nodules have not been shifted by metamorphic fluid, and thus can be used to infer the sulfur cycle during their formation.

The pyrite nodules display zonation patterns in both minor elements and sulfur isotope compositions, with high $\delta^{34}S$ and low $\Delta^{33}S$ values in the cores, an abrupt isotopic shift to high $\Delta^{33}S$ and negative $\delta^{34}S$ in the inner rims, and a continuous increase in $\Delta^{33}S$ and $\delta^{34}S$ values toward the outer rims. These patterns can be explained by addition and consumption of the abundant but short-lived FVA-like elemental sulfur during the time period of rim growth.

This study supports the hypothesis built on a previous study on pyrite nodules from the Joy Lake Sequence in the Superior Province that volcanic activity could affect the sulfur cycle in 2.7 Ga, at least for detectable temporal and spatial scales. An overview of previously published data in the Eastern Goldfields Superterrane implies that the volcanic effect may be widespread on a regional scale rather than limited to a local area.

7. Future work

To better understand some outstanding questions related to the sulfur cycle in the Archean, there is much additional work worth pursuing, in all perspectives of fieldwork, laboratory experiments, and theoretical modeling. A few ideas directly related to this study are highlighted below.

Firstly, to better constrain the spatial and temporal extents of the FVA signal, more samples are needed from the Eastern Goldfields Superterrane of the Yilgarn Craton. Most the FVA-like cases discussed in this study were obtained along the boundary of the Kalgoorlie and Kurnalpi Terranes. It is worth testing the distal extent of the volcanic effect. For example, whether the sedimentary pyrites from the west part of Kalgoorlie Terrane still contain the FVA-like signal would be interesting to study.

Secondly, laboratory experiments should be carried out focusing on pyrite formation with elemental sulfur and sulfide under different conditions. In this study, we proposed that the pyrite formation mechanism changed from sulfide pathway to polysulfide pathway during the growth from core to rim. However, the controlling factors that induced such a change are still unknown. Laboratory experiments with well-controlled pH, temperature or other conditions such as specific microorganism, and various elemental sulfur/sulfide ratios in the sulfur pool can be helpful to address this question.

.

8. References

Andres, R. and Kasgnoc, A. (1998) A time‐averaged inventory of subaerial volcanic sulfur emissions. Journal of Geophysical Research: Atmospheres 103, 25251-25261.

Archer, C. and Vance, D. (2006) Coupled Fe and S isotope evidence for Archean microbial Fe (III) and sulfate reduction. Geology 34, 153-156.

Archibald, N., Bettenay, L., Binns, R., Groves, D. and Gunthorpe, R. (1978) The evolution of Archaean greenstone terrains, Eastern Goldfields Province, Western Australia. Precambrian Research 6, 103-131.

Babikov, D. (2017) Recombination reactions as a possible mechanism of mass-independent fractionation of sulfur isotopes in the Archean atmosphere of Earth. Proceedings of the National Academy of Sciences 114, 3062-3067.

Babikov, D., Semenov, A. and Teplukhin, A. (2017) One possible source of mass-independent fractionation of sulfur isotopes in the Archean atmosphere of Earth. Geochim Cosmochim Ac 204, 388-406.

Barley, M.E., Brown, S.J., Krapež, B. and Kositcin, N. (2008) Physical volcanology and geochemistry of a Late Archaean volcanic arc: Kurnalpi and Gindalbie Terranes, Eastern Goldfields Superterrane, Western Australia. Precambrian Research 161, 53-76.

Barley, M.E., Eisenlohr, B.N., Groves, D.I., Perring, C.S. and Vearncombe, J.R. (1989) Late Archean convergent margin tectonics and gold mineralization: a new look at the Norseman-Wiluna Belt, Western Australia. Geology 17, 826-829.

Barnes, S.J. and Van Kranendonk, M.J. (2014) Archean andesites in the east Yilgarn craton, Australia: Products of plume-crust interaction? Lithosphere 6, 80-92.

Baroni, M., Thiemens, M.H., Delmas, R.J. and Savarino, J. (2007) Mass-independent sulfur isotopic compositions in stratospheric volcanic eruptions. Science 315, 84-87.

Beresford, S., Stone, W.E., Cas, R., Lahaye, Y. and Jane, M. (2005) Volcanological controls on the localization of the komatiite-hosted Ni-Cu-(PGE) Coronet deposit, Kambalda, Western Australia. Economic Geology 100, 1457-1467.

Blewett, R. and Czarnota, K. (2007) A new integrated tectonic framework of the Eastern Goldfields Superterrane. Geoscience Australia Record 14, 27-32.

Böttcher, M.E., Thamdrup, B. and Vennemann, T.W. (2001) Oxygen and sulfur isotope fractionation during anaerobic bacterial disproportionation of elemental sulfur. Geochim Cosmochim Ac 65, 1601-1609.

Brown, S., Barley, M., Krapež, B. and Cas, R. (2002) The Late Archaean Melita Complex, Eastern Goldfields, Western Australia: shallow submarine bimodal volcanism in a rifted arc environment. Journal of Volcanology and Geothermal Research 115, 303-327.

Butler, I.B., Böttcher, M.E., Rickard, D. and Oldroyd, A. (2004) Sulfur isotope partitioning during experimental formation of pyrite via the polysulfide and hydrogen sulfide pathways: implications for the interpretation of sedimentary and hydrothermal pyrite isotope records. Earth and Planetary Science Letters 228, 495-509.

Campbell, I., Griffiths, R. and Hill, R. (1989) Melting in an Archaean mantle plume: heads it's basalts, tails it's komatiites. Nature 339, 697-699.

Campbell, I. and Hill, R. (1988) A two-stage model for the formation of the granite-greenstone terrains of the Kalgoorlie-Norseman area, Western Australia. Earth and Planetary Science Letters 90, 11-25.

Canfield, D.E., Habicht, K.S. and Thamdrup, B. (2000) The Archean sulfur cycle and the early history of atmospheric oxygen. Science 288, 658-661.
Canfield, D.E. and Teske, A. (1996) Late Proterozoic rise in atmospheric oxygen concentration inferred from phylogenetic and sulphur-isotope studies. Nature 382, 127-132.
Canfield, D.E. and Thamdrup, B. (1994) The production of 34S-depleted sulfide during bacterial disproportionation of elemental sulfur. Science-AAAS-Weekly Paper Edition 266, 1973-1974.
Canfield, D.E., Thamdrup, B. and Fleischer, S. (1998) Isotope fractionation and sulfur metabolism by pure and enrichment cultures of elemental sulfur - disproportionating bacteria. Limnology and Oceanography 43, 253-264.
Chen, M., Campbell, I.H., Xue, Y., Tian, W., Ireland, T.R., Holden, P., Cas, R.A., Hayman, P.C. and Das, R. (2015) Multiple sulfur isotope analyses support a magmatic model for the volcanogenic massive sulfide deposits of the Teutonic Bore volcanic complex, Yilgarn Craton, Western Australia. Economic Geology 110, 1411-1423.
Claire, M.W., Kasting, J., Domagal-Goldman, S.D., Stüeken, E.E., Buick, R. and Meadows, V.S. (2014) Modeling the signature of sulfur mass-independent fractionation produced in the Archean atmosphere. Geochim. Cosmochim. Acta 141, 365-380.
Claoué-Long, J., Compston, W. and Cowden, A. (1988) The age of the Kambalda greenstones resolved by ion-microprobe: implications for Archaean dating methods. Earth and Planetary Science Letters 89, 239-259.
Condie, K.C. (1998) Episodic continental growth and supercontinents: a mantle avalanche connection? Earth and Planetary Science Letters 163, 97-108.
Crowe, S.A., Paris, G., Katsev, S., Jones, C., Kim, S.-T., Zerkle, A.L., Nomosatryo, S., Fowle, D.A., Adkins, J.F. and Sessions, A.L. (2014) Sulfate was a trace constituent of Archean seawater. Science 346, 735-739.
Czarnota, K., Champion, D., Goscombe, B., Blewett, R., Cassidy, K., Henson, P. and Groenewald, P. (2010) Geodynamics of the eastern Yilgarn Craton. Precambrian Research 183, 175-202.
Danielache, S.O., Eskebjerg, C., Johnson, M.S., Ueno, Y. and Yoshida, N. (2008) High - precision spectroscopy of 32S, 33S, and 34S sulfur dioxide: Ultraviolet absorption cross sections and isotope effects. Journal of Geophysical Research: Atmospheres (1984 - 2012) 113.
Domagal-Goldman, S.D., Kasting, J.F., Johnston, D.T. and Farquhar, J. (2008) Organic haze, glaciations and multiple sulfur isotopes in the Mid-Archean Era. Earth Planet. Sci. Lett. 269, 29-40.
Endo, Y., Danielache, S.O., Ueno, Y., Hattori, S., Johnson, M.S., Yoshida, N. and Kjaergaard, H.G. (2015) Photoabsorption cross - section measurements of 32S, 33S, 34S, and 36S sulfur dioxide from 190 to 220 nm. Journal of Geophysical Research: Atmospheres 120, 2546-2557.
Endo, Y., Ueno, Y., Aoyama, S. and Danielache, S.O. (2016) Sulfur isotope fractionation by broadband UV radiation to optically thin SO2 under reducing atmosphere. Earth and Planetary Science Letters 453, 9-22.
Farquhar, J., Bao, H. and Thiemens, M.H. (2000) Atmospheric influence of the Earth's earliest sulfur cycle. Science 289, 756-758.

Farquhar, J., Cliff, J., Zerkle, A.L., Kamyshny, A., Poulton, S.W., Claire, M., Adams, D., Harms, B. (2013) Pathways for Neoarchean pyrite formation constrained by mass-independent sulfur isotopes. PNAS 110, 17638-17643.

Farquhar, J., Peters, M., Johnston, D.T., Strauss, H., Masterson, A., Wiechert, U., Kaufman, A.J. (2007) Isotopic evidence for Mesoarchaean anoxia and changing atmospheric sulphur chemistry. Nature 449, 706-709.

Farquhar, J., Savarino, J., Airieau, S. and Thiemens, M.H. (2001) Observation of wavelength-sensitive mass-independent sulfur isotope effects during SO_2 photolysis: Applications to the early atmosphere. J. Geophys. Res. 106, 32829-32839.

Fisher, W.W., Fike, D.A., Johnson, J.E., Raub, T.D., Guan, Y., Kirschvink, J.L. and Eiler, J.M. (2014) SQUID–SIMS is a useful approach to uncover primary signals in the Archean sulfur cycle. PNAS 111, 5468-5473.

Gregory, D.D., Large, R.R., Halpin, J.A., Steadman, J.A., Hickman, A.H., Ireland, T.R., Holden, P. (2015) The chemical conditions of the late Archean Hamersley Basin inferred from whole rock and pyrite geochemistry with $\Delta^{33}S$ and $\delta^{34}S$ isotope analyses. Geochim. Cosmochim. Acta 149, 223-250.

Greig, D. (1984) Geology of the Teutonic Bore massive sulphide deposit, Western Australia. Australasian Institute of Mineralogy and Metallurgy Proceedings 289, 147-156.

Groves, D. and Batt, W. (1984) Spatial and temporal variations of Archaean metallogenic associations in terms of evolution of granitoid-greenstone terrains with particular emphasis on the Western Australian Shield, Archaean geochemistry. Springer, pp. 73-98.

Habicht, K., Gade, M., Thamdrup, B., Berg, P. and Canfield, D.E. (2002) Calibration of sulfate levels in the Archean Ocean. Science 298, 2372-2374.

Hallberg, J. (1986) Archaean basin development and crustal extension in the northeastern Yilgarn Block, Western Australia. Precambrian Research 31, 133-156.

Halmer, M., Schmincke, H.-U. and Graf, H.-F. (2002) The annual volcanic gas input into the atmosphere, in particular into the stratosphere: a global data set for the past 100 years. Journal of Volcanology and Geothermal Research 115, 511-528.

Heicklen, J., Kelly, N. and Partymiller, K. (1980) The photophysics and photochemistry of SO 2. Research on Chemical Intermediates 3, 315-404.

Hill, R.I., Chappell, B.W. and Campbell, I.H. (2011) Late Archaean granites of the southeastern Yilgarn Block, Western Australia: age, geochemistry, and origin. Earth and Environmental Science Transactions of the Royal Society of Edinburgh 83, 211-226.

Hofmann, A., Bekker, A., Rouxel, O.J., Rumble, D. and Master, S. (2009) Multiple sulphur and iron isotope composition of detrital pyrite in Archaean sedimentary rocks: A new tool for provenance analysis. Earth Planet. Sci. Lett. 286, 436-445.

Hollis, S.P., Mole, D.R., Gillespie, P., Barnes, S.J., Tessalina, S., Cas, R.A.F., Hildrew, C., Pumphrey, A., Goodz, M.D., Caruso, S., Yeats, C.J., Verbeeten, A., Belford, S.M., Wyche, S. and Martin, L.A.J. (2017) 2.7 Ga plume associated VHMS mineralization in the Eastern Goldfields Superterrane, Yilgarn Craton: Insights from the low temperature and shallow water, Ag-Zn-(Au) Nimbus deposit. Precambrian Research 291, 119-142.

Huston, D.L., Champion, D.C. and Cassidy, K.F. (2014) Tectonic controls on the endowment of Neoarchean cratons in volcanic-hosted massive sulfide deposits: evidence from lead and neodymium isotopes. Economic Geology 109, 11-26.

Izon, G., Zerkle, A.L., Zhelezinskaia, I., Farquhar, J., Newton, R.J., Poulton, S.W., Eigenbrode, J.L. and Claire, M.W. (2015) Multiple oscillations in Neoarchaean atmospheric chemistry. Earth Planet. Sci. Lett. 431, 264-273.

Jamieson, J.W., Wing, B.A., Farquhar, J. and Hannington, M.D. (2013) Neoarchean seawater sulfate concentrations from sulfur isotopes in Kidd Creek ore sulfides. Nature Geoscience 6, 61-64.

Johnston, D.T., Farquhar, J., Wing, B.A., Kaufman, A., Canfield, D.E. and Habicht, K.S. (2005a) Multiple sulfur isotope fractionations in biological systems: A case study with sulfate reducers and sulfur disproportionators. Amer. J. Sci. 305, 645-660.

Johnston, D.T., Farquhar, J., Canfield, D.E. (2007) Sulfur isotope insights into microbial sulfate reduction: When microbes meet models. Geochim. Cosmochim. Acta 71, 3929-3947.

Johnston, D.T., Wing, B.A., Farquhar, J., Kaufman, A.J., Strauss, H., Lyons, T.W., Kah, L.C. and Canfield, D.E. (2005b) Active microbial sulfur disproportionation in the Mesoproterozoic. Science 310, 1477-1479.

Kamber, B.S. and Whitehouse, M.J. (2007) Micro-scale sulphur isotope evidence for sulphur cycling in the late Archean shallow ocean. Geobiology 5, 5-17.

Kaufman, A., Johnston, D.T., Farquhar, J., Masterson, A.L., Lyons, T.W., Bates, S., Anbar, A., Arnold, G.L., Garvin, J. and Buick, R. (2007) Global biospheric oxygenation and atmospheric evolution at the close of the Archean Eon. Science 317, 1900-1903.

Kohn, M.J., Riciputi, L.R., Stakes, D. and Orange, D.L. (1998) Sulfur isotope variability in biogenic pyrite: Reflections of heterogeneous bacterial colonization? American Mineralogist 83, 1454-1468.

Kozdon, K., Kita, N.T., Huberty, J.M., Fournelle, J.H., Johnson, C.A. and Valley, J.W. (2010) In situ sulfur isotope analysis of sulfide minerals by SIMS: Precision and accuracy, with application to thermometry of ~3.5 Ga Pilbara cherts. Chem. Geol. 275, 243-253.

Krapez, B. (1997) Sequence - stratigraphic concepts applied to the identification of depositional basins and global tectonic cycles. Australian Journal of Earth Sciences 44, 1-36.

Krapež, B. and Hand, J.L. (2008) Late Archaean deep-marine volcaniclastic sedimentation in an arc-related basin: the Kalgoorlie Sequence of the Eastern Goldfields Superterrane, Yilgarn Craton, Western Australia. Precambrian Research 161, 89-113.

Kurzweil, F., Claire, M.W., Thomazo, C., Peters, M., Hannington, M.D. and Strauss, H. (2013) Atmospheric sulfur rearrangement 2.7 billion years ago: Evidence for oxygenic photosynthesis. Earth Planet. Sci. Lett. 366, 17-26.

Li, J., Zhang, Z., Stern, R.A., Hannah, J.L., Stein, H.J., Yang, G. and Li, L. (2017) Primary multiple sulfur isotopic compositions of pyrite in 2.7 Ga shales from the Joy Lake sequence (Superior Province) show felsic volcanic array-like signature. Geochim Cosmochim Ac.

Lyons, J.R. (2007) Mass-independent fractionation of sulfur isotopes by isotope-selective photodissociation of SO_2. Geophys. Res. Lett. 34, L22811.

Lyons, J.R. (2008) Photolysis of long-lived predissociative molecules as a source of mass-independent isotope fractionation: The example of SO 2. Advances in Quantum Chemistry 55, 57-74.

MacLean, P.J. and Fleet, M.E. (1989) Detrital pyrite in the Witwatersrand gold fields of South Africa; evidence from truncated growth banding. Economic Geology 84, 2008-2011.

Marin-Carbonne, J., Rollion-Bard, C., Bekker, A., Rouxel, O., Agangi, A., Cavalazzi, B., Wohlgemuth-Ueberwasser, C.C., Hofmann, A. and McKeegan, K.D. (2014) Coupled Fe

and S isotope variations in pyrite nodules from Archean shale. Earth Planet. Sci. Lett. 392, 67-79.
Masterson, A.W., Farquhar, J. and Wing, B.A. (2011) Sulfur mass-independent fractionation patterns in the broadband UV photolysis of sulfur dioxide: pressure and third body effects. Earth Planet. Sci. Lett. 306, 253-260.
Mishima, K., Yamazaki, R., Satish-Kumar, M., Ueno, Y., Hokada, T., Toyoshima, T. (2017) Multiple sulfur isotope geochemistry of Dharwar Supergroup, Southern India: Late Archean record of changing atmospheric chemistry. Earth Planet. Sci. Lett. 464, 69-83.
Morris, P. and Witt, W. (1997) Geochemistry and tectonic setting of two contrasting Archaean felsic volcanic associations in the Eastern Goldfields, Western Australia. Precambrian Research 83, 83-107.
Muller, É., Philippot, P., Rollion-Bard, C. and Cartigny, P. (2016) Multiple sulfur-isotope signatures in Archean sulfates and their implications for the chemistry and dynamics of the early atmosphere. Proceedings of the National Academy of Sciences 113, 7432-7437.
Oduro, H., Harms, B., Sintim, H.O., Kaufman, A.J., Cody, G. and Farquhar, J. (2011) Evidence of magnetic isotope effects during thermochemical sulfate reduction. PNAS 108, 17635-17638.
Ohmoto, H., Watanabe, Y., Ikemi, H., Poulson, S.R. and Taylor, B.E. (2006) Sulphur isotope evidence for an oxic Archaean atmosphere. Nature 442, 908-911.
Ono, S., Beukes, N.J., Rumble, D. (2009) Origin of two distinct multiple-sulfur isotope compositions of pyrite in the 2.5 Ga Klein Naute Formation, Griqualand West Basin, South Africa. Precam. Res. 169, 48-57.
Ono, S., Eigenbrode, J.L., Pavlov, A.A., Kharecha, P., Rumble, D., Kasting, J.F. and Freeman, K.H. (2003) New insights into Archean sulfur cycle from mass-independent sulfur isotope records from the Hamersley Basin, Australia. Earth Planet. Sci. Lett. 213, 15-30.
Ono, S., Whitehill, A.R. and Lyons, J.R. (2013) Contribution of isotopologue self-shielding to sulfur mass-independent fractionation during sulfur dioxide photolysis. J. Geophys. Res. 118, 1-11.
Pavlov, A. and Kasting, J. (2002) Mass-independent fractionation of sulfur isotopes in Archean sediments: strong evidence for an anoxic Archean atmosphere. Astrobiology 2, 27-41.
Peters, M., Strauss, H., Farquhar, J., Ockert, C., Eickmann, B. and Jost, C.L. (2010) Sulfur cycling at the Mid-Atlantic Ridge: A multiple sulfur isotope approach. Chemical Geology 269, 180-196.
Philippot, P., Van Zuilen, M. and Rollion-Bard, C. (2012) Variations in atmospheric sulphur chemistry on early Earth linked to volcanic activity. Nature Geoscience 5, 668-674.
Rickard, D. (2012) Sulfidic sediments and sedimentary rocks. Newnes.
Said, N., Kerrich, R. and Groves, D. (2010) Geochemical systematics of basalts of the Lower Basalt Unit, 2.7 Ga Kambalda Sequence, Yilgarn Craton, Australia: Plume impingement at a rifted craton margin. Lithos 115, 82-100.
Sarka, K., Danielache, S.O., Kondorskiy, A. and Nanbu, S. (2017) Theoretical study of electronic properties and isotope effects in the UV absorption spectrum of disulfur. Chemical Physics 488–489, 36-42.
Savarino, J., Romero, A., Cole-Dai, J., Bekki, S. and Thiemens, M.H. (2003) UV induced mass-independent sulfur isotope fractionation in stratospheric volcanic sulfate. Geophys. Res. Lett. 30, 2131.

Steadman, J.A., Large, R.R., Meffre, S., Olin, P.H., Danyushevsky, L.V., Gregory, D.D., Belousov, I., Lounejeva, E., Ireland, T.R. and Holden, P. (2015) Synsedimentary to early diagenetic gold in black shale-hosted pyrite nodules at the Golden Mile Deposit, Kalgoorlie, Western Australia. Economic Geology 110, 1157-1191.

Surkov, A.V., Böttcher, M.E. and Kuever, J. (2012) Sulphur isotope fractionation during the reduction of elemental sulphur and thiosulphate by Dethiosulfovibrio spp. Isotopes in Environmental and Health Studies, 48, 65-75.

Swager, C. (1997) Tectono-stratigraphy of late Archaean greenstone terranes in the southern Eastern Goldfields, Western Australia. Precambrian Research 83, 11-42.

Swager, C. and Griffin, T.J. (1990) An early thrust duplex in the Kalgoorlie-Kambalda greenstone belt, Eastern Goldfields Province, Western Australia. Precambrian Research 48, 63-73.

Swager, C., Witt, W., Griffin, T., Ahmat, A., Hunter, W., McGoldrick, P. and Wyche, S. (1992) Late Archaean granite-greenstones of the Kalgoorlie Terrane, Yilgarn Craton, Western Australia. The Archaean: terrains, processes and metallogeny 22, 107-122.

Thomazo, C., Ader, M., Farquhar, J. and Philippot, P. (2009) Methanotrophs regulated atmospheric sulfur isotope anomalies during the Mesoarchean (Tumbiana Formation, Western Australia). Earth Planet. Sci. Lett. 279, 65-75.

Þórðarson, Þ. and Self, S. (2001) Real–time observations of the Laki sulfuric aerosol cloud in Europe during 1783 as documented by Professor SP van Swinden at Franeker, Holland. Jökull 50, 65-72.

Ueno, Y., Johnson, M.S., Danielache, S.O., Eskebjerg, C., Pandey, A. and Yoshida, N. (2009) Geological sulfur isotopes indicate elevated OCS in the Archean atmosphere, solving faint young sun paradox. PNAS 106, 14784-14789.

Watanabe, Y., Farquhar, J. and Ohmoto, H. (2009) Anomalous fractionations of sulfur isotopes during thermochemical sulfate reduction. Science 324, 370-373.

Whitehill, A.R. and Ono, S. (2012) Excitation band dependence of sulfur isotope mass-independent fractionation during photochemistry of sulfur dioxide using broadband light sources. Geochim. Cosmochim. Acta 94, 238-253.

Whitehill, A.R., Xie, C., Hu, X., Xie, D., Guo, H., Ono, S. (2013) Vibronic origin of sulfur mass-independent isotope effect in photoexcitation of SO2 and the implications to the early earth's atmosphere. PNAS 110, 17697-17702.

Williford, K.H., Ushikubo, T., Lepot, K., Kitajima, K., Hallmann, C., Spicuzza, M.J., Kozdon, R., Eigenbrode, J.L., Summons, R.E. and Valley, J.W. (2016) Carbon and sulfur isotopic signatures of ancient life and environment at the microbial scale: Neoarchean shales and carbonates. Geobiology 14, 105-128.

Williford, K.H., Van Kranendonk, M.J., Ushikubo, T., Kozdon, R. and Valley, J.W. (2011) Constraining atmospheric oxygen and seawater sulfate concentrations during Paleoproterozoic glaciation: In situ sulfur three-isotope microanalysis of pyrite from the Turee Creek Group, Western Australia. Geochim. Cosmochim. Acta 75, 5686-5705.

Zerkle, A.L., Claire, M.W., Domagal-Goldman, S.D., Farquhar, J. and Poulson, S.W. (2012) A bistable organic-rich atmosphere on the Neoarchaean Earth. Nature Geoscience 5, 359-363.

Table 1. Major and minor elements of pyrite from Nimbus deposit, West Australia

Sample	Co wt%	2σ (%)	Ni wt%	2σ (%)	Cu wt%	2σ (%)	Fe wt%	2σ (%)	S wt%	2σ (%)	Total (wt%)
Nodule 1-XS-1	BDL	BDL	0.03	0.01	BDL	BDL	45.32	0.15	52.78	0.19	98.18
Nodule 1-XS-2	BDL	BDL	BDL	BDL	BDL	BDL	45.83	0.15	53.14	0.19	98.99
Nodule 1-XS-3	BDL	BDL	BDL	BDL	BDL	BDL	46.03	0.15	53.31	0.19	99.34
Nodule 1-XS-4	BDL	BDL	BDL	BDL	BDL	BDL	46.09	0.15	53.47	0.19	99.56
Nodule 1-XS-5	BDL	BDL	BDL	BDL	BDL	BDL	46.23	0.15	53.52	0.19	99.75
Nodule 1-XS-6	BDL	BDL	BDL	BDL	BDL	BDL	46.21	0.15	53.52	0.19	99.73
Nodule 1-XS-7	BDL	BDL	BDL	BDL	BDL	BDL	46.36	0.15	53.52	0.19	99.88
Nodule 1-XS-8	BDL	BDL	BDL	BDL	BDL	BDL	46.29	0.15	53.65	0.19	99.94
Nodule 1-XS-9	BDL	BDL	0.01	0.01	BDL	BDL	46.39	0.15	53.41	0.19	99.81
Nodule 1-XS-10	BDL	BDL	BDL	BDL	0.01	0.01	46.19	0.15	53.53	0.19	99.73
Nodule 1-XS-11	BDL	BDL	BDL	BDL	0.02	0.01	46.17	0.15	53.56	0.19	99.74
Nodule 1-XS-12	BDL	BDL	BDL	BDL	BDL	BDL	46.24	0.15	53.55	0.19	99.79
Nodule 1-XS-13	BDL	BDL	BDL	BDL	0.01	0.01	46.15	0.15	53.36	0.19	99.53
Nodule 1-XS-14	BDL	BDL	0.08	0.01	0.02	0.01	45.70	0.15	53.15	0.19	98.94
Nodule 1-XS-15	BDL	BDL	0.08	0.01	0.02	0.01	45.86	0.15	53.01	0.19	98.97
Nodule 1-XS-16	BDL	BDL	0.07	0.01	0.03	0.01	45.85	0.15	52.61	0.19	98.56
Nodule 1-XS-17	BDL	BDL	0.07	0.01	0.02	0.01	46.09	0.15	52.98	0.19	99.22
Nodule 1-XS-18	BDL	BDL	0.08	0.01	0.04	0.01	46.19	0.15	53.18	0.19	99.49
Nodule 1-XS-19	BDL	BDL	0.09	0.01	0.02	0.01	45.96	0.15	52.74	0.19	98.81
Nodule 1-XS-20	BDL	BDL	0.07	0.01	BDL	BDL	45.94	0.15	52.67	0.19	98.68
Nodule 1-XS-21	BDL	BDL	0.10	0.01	0.03	0.01	46.03	0.15	52.94	0.19	99.09
Nodule 1-XS-22	BDL	BDL	0.11	0.01	0.03	0.01	46.03	0.15	52.86	0.19	99.03
Nodule 1-XS-23	BDL	BDL	0.11	0.01	0.03	0.01	45.75	0.15	52.72	0.19	98.60
Nodule 1-XS-24	BDL	BDL	0.08	0.01	0.04	0.01	45.65	0.15	52.80	0.19	98.57
Nodule 1-XS-25	BDL	BDL	0.07	0.01	0.03	0.01	45.65	0.15	52.72	0.19	98.47
Nodule 1-XS-26	BDL	BDL	0.10	0.01	0.03	0.01	45.83	0.15	53.00	0.19	98.96
Nodule 1-XS-27	BDL	BDL	0.10	0.01	0.04	0.01	45.77	0.15	52.62	0.19	98.53
Nodule 1-XS-28	BDL	BDL	0.10	0.01	BDL	BDL	45.92	0.15	52.69	0.19	98.71
Nodule 1-XS-29	BDL	BDL	0.11	0.01	0.04	0.01	45.61	0.15	52.61	0.19	98.36

Sample	Co wt%	2σ (%)	Ni wt%	2σ (%)	Cu wt%	2σ (%)	Fe wt%	2σ (%)	S wt%	2σ (%)	Total (wt%)
Nodule 1-XS-30	BDL	BDL	0.12	0.01	0.04	0.01	45.59	0.15	52.46	0.19	98.21
Nodule 1-XS-31	BDL	BDL	0.12	0.01	0.03	0.01	45.89	0.15	52.97	0.19	99.01
Nodule 1-XS-32	BDL	BDL	0.12	0.01	0.02	0.01	45.73	0.15	52.65	0.19	98.52
Nodule 1-XS-33	BDL	BDL	0.11	0.01	0.04	0.01	45.73	0.15	52.79	0.19	98.67
Nodule 1-XS-34	BDL	BDL	0.11	0.01	0.04	0.01	45.64	0.15	52.43	0.19	98.22
Nodule 1-XS-35	BDL	BDL	0.13	0.01	0.06	0.01	45.38	0.15	52.44	0.19	98.01
Nodule 1-XS-36	BDL	BDL	0.12	0.01	0.05	0.01	45.60	0.15	52.23	0.19	97.99
Nodule 1-XS-37	BDL	BDL	0.14	0.01	0.04	0.01	45.49	0.15	52.34	0.19	98.01
Nodule 1-XS-38	BDL	BDL	0.11	0.01	0.06	0.01	45.25	0.14	52.01	0.19	97.43
Nodule 1-XS-39	0.02	0.01	0.04	0.01	0.03	0.01	45.34	0.15	52.42	0.19	97.84
Nodule 1-XS-40	BDL	BDL	0.14	0.01	0.05	0.01	45.08	0.14	52.14	0.19	97.41
Nodule 1-XS-41	BDL	BDL	0.11	0.01	0.05	0.01	45.08	0.14	52.27	0.19	97.51
Nodule 1-XS-42	0.02	0.01	0.11	0.01	0.04	0.01	45.03	0.14	52.48	0.19	97.67
Nodule 1-XS-43	BDL	BDL	0.12	0.01	0.04	0.01	45.07	0.14	52.50	0.19	97.75
Nodule 1-XS-44	0.02	0.01	0.12	0.01	0.04	0.01	45.16	0.14	52.31	0.19	97.65
Nodule 1-XS-45	BDL	BDL	0.12	0.01	0.04	0.01	45.25	0.14	52.35	0.19	97.75
Nodule 1-XS-46	BDL	BDL	0.13	0.01	0.03	0.01	45.23	0.14	52.03	0.19	97.42
Nodule 1-XS-47	BDL	BDL	0.10	0.01	0.04	0.01	45.24	0.14	52.40	0.19	97.79
Nodule 1-XS-48	BDL	BDL	0.04	0.01	0.02	0.01	46.38	0.15	53.52	0.19	99.94
Nodule 1-XS-49	BDL	BDL	0.09	0.01	0.03	0.01	45.34	0.14	52.39	0.19	97.85
Nodule 1-XS-50	0.02	0.01	0.09	0.01	0.03	0.01	45.36	0.14	52.43	0.19	97.93
Nodule 1-XS-51	BDL	BDL	0.08	0.01	0.03	0.01	45.14	0.14	51.83	0.19	97.10
Nodule 1-XS-52	BDL	BDL	0.10	0.01	0.04	0.01	44.94	0.14	51.88	0.19	96.96
Nodule 1-XS-53	BDL	BDL	0.08	0.01	0.04	0.01	45.09	0.14	52.15	0.19	97.36
Nodule 1-XS-54	BDL	BDL	0.08	0.01	0.04	0.01	45.74	0.15	52.59	0.19	98.46
Nodule 1-XS-55	BDL	BDL	0.10	0.01	0.04	0.01	44.89	0.14	50.34	0.19	95.59
Nodule 1-XS-56	BDL	BDL	0.13	0.01	0.05	0.01	44.89	0.14	52.18	0.19	97.29
Nodule 1-XS-57	BDL	BDL	0.10	0.01	0.04	0.01	45.00	0.14	52.24	0.19	97.38
Nodule 1-XS-58	0.02	0.01	0.07	0.01	0.03	0.01	45.21	0.14	52.19	0.19	97.52
Nodule 1-XS-59	BDL	BDL	0.10	0.01	0.04	0.01	45.17	0.14	52.32	0.19	97.63
Nodule 1-XS-60	BDL	BDL	0.09	0.01	0.04	0.01	45.31	0.14	52.11	0.19	97.56

Sample	Co wt%	2σ (%)	Ni wt%	2σ (%)	Cu wt%	2σ (%)	Fe wt%	2σ (%)	S wt%	2σ (%)	Total (wt%)
Nodule 1-XS-61	BDL	BDL	0.11	0.01	0.04	0.01	45.36	0.14	52.38	0.19	97.88
Nodule 1-XS-62	BDL	BDL	0.10	0.01	0.03	0.01	46.11	0.15	53.82	0.19	100.06
Nodule 1-XS-63	BDL	BDL	0.12	0.01	0.04	0.01	45.08	0.14	51.59	0.19	96.84
Nodule 1-XS-64	BDL	BDL	0.13	0.01	0.03	0.01	45.47	0.15	52.70	0.19	98.32
Nodule 1-XS-65	BDL	BDL	0.11	0.01	0.03	0.01	45.46	0.15	52.68	0.19	98.28
Nodule 1-XS-66	BDL	BDL	0.11	0.01	0.03	0.01	45.57	0.15	52.60	0.19	98.32
Nodule 1-XS-67	BDL	BDL	0.11	0.01	0.04	0.01	45.48	0.15	52.62	0.19	98.25
Nodule 1-XS-68	BDL	BDL	0.12	0.01	0.04	0.01	45.49	0.15	52.48	0.19	98.13
Nodule 1-XS-69	BDL	BDL	0.11	0.01	0.04	0.01	45.33	0.14	52.48	0.19	97.96
Nodule 1-XS-70	BDL	BDL	0.09	0.01	0.03	0.01	45.56	0.15	53.05	0.19	98.73
Nodule 1-XS-71	BDL	BDL	0.08	0.01	0.02	0.01	45.56	0.15	52.58	0.19	98.25
Nodule 1-XS-72	BDL	BDL	0.08	0.01	0.06	0.01	45.90	0.15	52.63	0.19	98.67
Nodule 1-XS-73	BDL	BDL	0.05	0.01	0.03	0.01	45.43	0.14	52.61	0.19	98.12
Nodule 1-XS-74	BDL	BDL	0.11	0.01	0.04	0.01	45.91	0.15	52.86	0.19	98.93
Nodule 1-XS-75	BDL	BDL	0.09	0.01	0.02	0.01	46.05	0.15	53.01	0.19	99.17
Nodule 1-XS-76	BDL	BDL	0.07	0.01	0.03	0.01	46.15	0.15	53.15	0.19	99.40
Nodule 1-XS-77	BDL	BDL	0.09	0.01	0.02	0.01	46.02	0.15	53.28	0.19	99.40
Nodule 1-XS-78	BDL	BDL	0.09	0.01	0.03	0.01	45.98	0.15	53.22	0.19	99.32
Nodule 1-XS-79	BDL	BDL	0.10	0.01	0.02	0.01	45.95	0.15	53.09	0.19	99.16
Nodule 1-XS-80	BDL	BDL	0.02	0.01	BDL	BDL	45.85	0.15	53.11	0.19	98.98
Nodule 1-XS-81	BDL	BDL	0.06	0.01	0.02	0.01	45.95	0.15	53.13	0.19	99.17
Nodule 1-XS-82	BDL	BDL	0.05	0.01	0.02	0.01	45.99	0.15	53.18	0.19	99.25
Nodule 1-XS-83	BDL	BDL	0.06	0.01	0.02	0.01	45.87	0.15	53.13	0.19	99.13
Nodule 1-XS-84	BDL	BDL	0.07	0.01	0.02	0.01	45.87	0.15	53.48	0.19	99.44
Nodule 1-XS-85	BDL	BDL	BDL	BDL	BDL	BDL	46.09	0.15	53.45	0.19	99.54
Nodule 1-XS-86	BDL	BDL	BDL	BDL	BDL	BDL	46.21	0.15	53.82	0.19	100.03
Nodule 1-XS-87	BDL	BDL	BDL	BDL	0.02	0.01	45.81	0.15	52.91	0.19	98.80
Nodule 1-XS-88	BDL	BDL	0.04	0.01	BDL	BDL	45.96	0.15	53.33	0.19	99.33
Nodule 1-XS-89	BDL	BDL	0.02	0.01	0.01	0.01	46.09	0.15	53.34	0.19	99.47
Nodule 1-XS-90	BDL	BDL	BDL	BDL	BDL	BDL	46.49	0.15	53.87	0.19	100.36
Nodule 1-XS-91	BDL	BDL	BDL	BDL	0.01	0.01	46.48	0.15	53.13	0.19	99.63

Sample	Co wt%	2σ (%)	Ni wt%	2σ (%)	Cu wt%	2σ (%)	Fe wt%	2σ (%)	S wt%	2σ (%)	Total (wt%)
Nodule 1-XS-92	BDL	BDL	BDL	BDL	0.02	0.01	46.73	0.15	54.00	0.19	100.75
Nodule 1-XS-93	BDL	BDL	0.01	0.01	BDL	BDL	47.02	0.15	54.05	0.19	101.09
Nodule 1-XS-94	BDL	BDL	BDL	BDL	BDL	BDL	46.58	0.15	53.81	0.19	100.39
Nodule 1-XS-95	BDL	BDL	BDL	BDL	BDL	BDL	46.78	0.15	53.88	0.19	100.65
Nodule 1-XS-96	BDL	BDL	0.02	0.01	BDL	BDL	46.23	0.15	53.60	0.19	99.85
Nodule 1-XS-97	BDL	BDL	BDL	BDL	BDL	BDL	46.29	0.15	53.79	0.19	100.08
Nodule 1-XS-98	BDL	BDL	BDL	BDL	BDL	BDL	46.21	0.15	53.64	0.19	99.85
Nodule 1-XS-99	BDL	BDL	0.02	0.01	BDL	BDL	46.28	0.15	53.97	0.19	100.26
Nodule 1-XS-100	BDL	BDL	BDL	BDL	BDL	BDL	46.05	0.15	53.80	0.19	99.85
Nodule 2-XS-1	BDL	BDL	0.20	0.01	BDL	BDL	45.36	0.14	52.81	0.19	98.37
Nodule 2-XS-2	BDL	BDL	0.15	0.01	BDL	BDL	45.49	0.14	52.92	0.19	98.56
Nodule 2-XS-3	BDL	BDL	0.21	0.02	BDL	BDL	45.39	0.14	52.74	0.19	98.34
Nodule 2-XS-4	BDL	BDL	0.14	0.01	BDL	BDL	45.42	0.14	52.87	0.19	98.42
Nodule 2-XS-5	BDL	BDL	0.26	0.02	BDL	BDL	45.31	0.14	52.54	0.19	98.11
Nodule 2-XS-6	BDL	BDL	0.10	0.01	0.25	0.02	44.56	0.14	51.65	0.19	96.56
Nodule 2-XS-7	BDL	BDL	0.11	0.01	BDL	BDL	46.00	0.15	53.26	0.19	99.36
Nodule 2-XS-8	BDL	BDL	0.17	0.01	0.02	0.01	45.73	0.14	52.35	0.19	98.28
Nodule 2-XS-9	BDL	BDL	0.09	0.01	4.22	0.04	43.92	0.14	51.16	0.19	99.44
Nodule 2-XS-10	BDL	BDL	0.18	0.01	BDL	BDL	46.25	0.15	53.57	0.19	100.00
Nodule 2-XS-11	BDL	BDL	0.25	0.02	0.02	0.01	45.08	0.14	52.34	0.19	97.69
Nodule 2-XS-12	0.04	0.01	0.28	0.02	0.02	0.01	45.55	0.14	52.75	0.19	98.64
Nodule 2-XS-13	BDL	BDL	0.22	0.01	BDL	BDL	45.27	0.14	52.55	0.19	98.05
Nodule 2-XS-14	0.02	0.01	0.21	0.02	BDL	BDL	45.20	0.14	52.55	0.19	97.99
Nodule 2-XS-15	0.03	0.01	0.18	0.01	0.02	0.01	45.22	0.14	52.32	0.19	97.83
Nodule 2-XS-16	0.04	0.01	0.24	0.02	0.02	0.01	45.27	0.14	52.41	0.19	97.97
Nodule 2-XS-17	0.03	0.01	0.18	0.01	0.05	0.01	44.99	0.14	52.37	0.19	97.62
Nodule 2-XS-18	0.05	0.01	0.24	0.02	0.02	0.01	44.77	0.14	52.28	0.19	97.35
Nodule 2-XS-19	0.08	0.01	0.26	0.02	BDL	BDL	44.80	0.14	52.15	0.19	97.29
Nodule 2-XS-20	0.05	0.01	0.25	0.02	BDL	BDL	45.12	0.14	51.43	0.19	96.86
Nodule 2-XS-21	0.08	0.01	0.14	0.01	0.93	0.02	43.88	0.14	51.26	0.19	96.31

Sample	Co wt%	2σ (%)	Ni wt%	2σ (%)	Cu wt%	2σ (%)	Fe wt%	2σ (%)	S wt%	2σ (%)	Total (wt%)
Nodule 2-XS-22	0.05	0.01	0.22	0.01	0.02	0.01	44.76	0.14	52.11	0.19	97.16
Nodule 2-XS-23	0.03	0.01	0.13	0.01	0.02	0.01	44.95	0.14	52.38	0.19	97.51
Nodule 2-XS-24	0.05	0.01	0.23	0.02	BDL	BDL	45.13	0.14	52.29	0.19	97.70
Nodule 2-XS-25	0.06	0.01	0.19	0.01	0.02	0.01	44.97	0.14	52.19	0.19	97.42
Nodule 2-XS-26	0.04	0.01	0.22	0.02	0.02	0.01	45.11	0.14	52.27	0.19	97.66
Nodule 2-XS-27	0.04	0.01	0.36	0.02	BDL	BDL	44.80	0.14	52.17	0.19	97.37
Nodule 2-XS-28	0.04	0.01	0.21	0.01	BDL	BDL	45.21	0.14	52.36	0.19	97.82
Nodule 2-XS-29	0.03	0.01	0.19	0.01	BDL	BDL	45.33	0.14	52.56	0.19	98.11
Nodule 2-XS-30	BDL	BDL	0.22	0.01	0.02	0.01	45.40	0.14	53.07	0.19	98.71
Nodule 2-XS-31	BDL	BDL	0.25	0.02	BDL	BDL	45.37	0.14	52.74	0.19	98.37
Nodule 2-XS-32	0.02	0.01	0.20	0.01	BDL	BDL	45.33	0.14	52.64	0.19	98.18
Nodule 2-XS-33	0.02	0.01	0.23	0.02	BDL	BDL	45.22	0.14	52.43	0.19	97.90
Nodule 2-XS-34	0.04	0.01	0.23	0.02	BDL	BDL	45.33	0.14	52.59	0.19	98.18
Nodule 2-XS-35	BDL	BDL	0.25	0.02	BDL	BDL	45.33	0.14	52.61	0.19	98.20
Nodule 2-XS-36	0.02	0.01	0.16	0.01	0.02	0.01	45.25	0.14	52.51	0.19	97.96
Nodule 2-XS-37	BDL	BDL	0.25	0.02	BDL	BDL	45.18	0.14	52.77	0.19	98.19
Nodule 2-XS-38	BDL	BDL	0.23	0.02	BDL	BDL	45.51	0.14	52.72	0.19	98.45
Nodule 2-XS-39	BDL	BDL	0.09	0.01	BDL	BDL	45.72	0.14	52.89	0.19	98.69
Nodule 2-XS-40	BDL	BDL	0.19	0.01	BDL	BDL	45.56	0.14	52.82	0.19	98.58
Nodule 2-XS-41	BDL	BDL	0.18	0.01	BDL	BDL	45.54	0.14	52.70	0.19	98.42
Nodule 2-XS-42	BDL	BDL	0.14	0.01	0.02	0.01	45.60	0.14	53.01	0.19	98.76
Nodule 2-XS-43	BDL	BDL	0.20	0.01	BDL	BDL	45.47	0.14	52.84	0.19	98.51
Nodule 2-XS-44	BDL	BDL	0.13	0.01	BDL	BDL	45.75	0.14	53.07	0.19	98.95
Nodule 2-XS-45	BDL	BDL	0.22	0.02	BDL	BDL	45.51	0.14	53.12	0.19	98.86
Nodule 2-XS-46	BDL	BDL	0.15	0.01	BDL	BDL	45.59	0.14	53.08	0.19	98.82
Nodule 2-XS-47	BDL	BDL	BDL	BDL	0.02	0.01	45.92	0.15	53.55	0.19	99.49
Nodule 2-XS-48	BDL	BDL	BDL	BDL	BDL	BDL	46.14	0.15	53.56	0.19	99.74
Nodule 2-XS-49	BDL	BDL	0.02	0.01	0.02	0.01	46.01	0.15	53.61	0.19	99.65
Nodule 2-XS-50	BDL	BDL	BDL	BDL	BDL	BDL	46.07	0.15	53.50	0.19	99.57
Subhedral pyrite-1	BDL	BDL	0.08	0.01	BDL	BDL	46.03	0.15	53.95	0.19	100.06

Sample	Co wt%	2σ (%)	Ni wt%	2σ (%)	Cu wt%	2σ (%)	Fe wt%	2σ (%)	S wt%	2σ (%)	Total (wt%)
Subhedral pyrite-2	BDL	BDL	0.10	0.01	BDL	BDL	46.22	0.15	53.78	0.19	100.10
Subhedral pyrite-3	BDL	BDL	0.10	0.01	BDL	BDL	46.33	0.15	53.91	0.19	100.34
Subhedral pyrite-4	BDL	BDL	0.10	0.01	BDL	BDL	46.43	0.15	53.94	0.19	100.46
Subhedral pyrite-5	BDL	BDL	0.07	0.01	BDL	BDL	46.56	0.15	53.59	0.19	100.22
Subhedral pyrite-6	BDL	BDL	0.06	0.01	BDL	BDL	46.64	0.15	54.00	0.19	100.69
Subhedral pyrite-7	BDL	BDL	0.08	0.01	BDL	BDL	46.64	0.15	53.86	0.19	100.58
Subhedral pyrite-8	BDL	BDL	0.08	0.01	BDL	BDL	46.55	0.15	54.02	0.19	100.65
Subhedral pyrite-9	BDL	BDL	0.07	0.01	BDL	BDL	46.32	0.15	53.84	0.19	100.25
Subhedral pyrite-10	BDL	BDL	0.07	0.01	BDL	BDL	46.22	0.15	53.87	0.19	100.17
Subhedral pyrite-11	BDL	BDL	0.12	0.01	BDL	BDL	46.07	0.15	53.76	0.19	99.95
Subhedral pyrite-12	BDL	BDL	0.05	0.01	BDL	BDL	46.18	0.15	53.80	0.19	100.03
Subhedral pyrite-13	0.06	0.01	0.08	0.01	BDL	BDL	46.22	0.15	53.98	0.19	100.34
Subhedral pyrite-14	0.02	0.01	0.02	0.01	BDL	BDL	46.27	0.15	53.95	0.19	100.25
Subhedral pyrite-15	0.02	0.01	0.07	0.01	0.02	0.01	46.34	0.15	53.82	0.19	100.27
Subhedral pyrite-16	0.03	0.01	0.04	0.01	BDL	BDL	46.33	0.15	53.94	0.19	100.33
Subhedral pyrite-17	BDL	BDL	0.05	0.01	BDL	BDL	46.04	0.15	53.87	0.19	100.00
Subhedral pyrite-18	BDL	BDL	0.03	0.01	0.02	0.01	45.87	0.15	53.59	0.19	99.53
Subhedral pyrite-19	BDL	BDL	0.06	0.01	BDL	BDL	46.17	0.15	53.80	0.19	100.05
Subhedral pyrite-20	BDL	BDL	BDL	BDL	BDL	BDL	45.90	0.15	53.71	0.19	99.72
Subhedral pyrite-21	0.04	0.01	0.10	0.01	BDL	BDL	46.18	0.15	53.93	0.19	100.26
Subhedral pyrite-22	BDL	BDL	0.05	0.01	BDL	BDL	46.14	0.15	53.76	0.19	99.97
Subhedral pyrite-23	BDL	BDL	BDL	BDL	BDL	BDL	46.25	0.15	53.90	0.19	100.15
Subhedral pyrite-24	BDL	BDL	0.04	0.01	BDL	BDL	45.94	0.15	54.00	0.19	99.97
Subhedral pyrite-25	BDL	BDL	0.09	0.01	BDL	BDL	46.28	0.15	53.89	0.19	100.25
Subhedral pyrite-26	BDL	BDL	0.08	0.01	BDL	BDL	46.05	0.15	53.57	0.19	99.70
Subhedral pyrite-27	BDL	BDL	0.09	0.01	BDL	BDL	46.13	0.15	53.94	0.19	100.16
Subhedral pyrite-28	BDL	BDL	0.10	0.01	BDL	BDL	46.04	0.15	53.58	0.19	99.73
Subhedral pyrite-29	BDL	BDL	0.08	0.01	BDL	BDL	46.21	0.15	53.78	0.19	100.07
Subhedral pyrite-30	BDL	BDL	0.07	0.01	BDL	BDL	46.30	0.15	53.73	0.19	100.11
Subhedral pyrite-31	BDL	BDL	0.07	0.01	BDL	BDL	46.31	0.15	53.90	0.19	100.28
Subhedral pyrite-32	BDL	BDL	0.08	0.01	BDL	BDL	46.25	0.15	53.88	0.19	100.21

Sample	Co wt%	2σ (%)	Ni wt%	2σ (%)	Cu wt%	2σ (%)	Fe wt%	2σ (%)	S wt%	2σ (%)	Total (wt%)
Subhedral pyrite-33	BDL	BDL	0.03	0.01	BDL	BDL	46.31	0.15	53.87	0.19	100.20
Subhedral pyrite-34	BDL	BDL	0.03	0.01	BDL	BDL	46.65	0.15	53.94	0.19	100.62
Subhedral pyrite-35	BDL	BDL	0.06	0.01	BDL	BDL	46.37	0.15	53.92	0.19	100.35
Subhedral pyrite-36	BDL	BDL	BDL	BDL	BDL	BDL	46.29	0.15	53.82	0.19	100.12

*BDL denotes concentrations are below detection limits

Table 2. Multiple sulfur isotopes of pyrite from Nimbus deposit, West Australia

Sample	$\delta^{34}S_{(VCDT)}$ (‰)	2σ (‰)	$\Delta^{33}S$ (‰)	2σ (‰)	$\Delta^{36}S$ (‰)	2σ (‰)
Nodule 1-XS-1	0.89	0.11	3.40	0.08	-1.63	0.80
Nodule 1-XS-2	0.82	0.11	3.08	0.09	-1.79	0.59
Nodule 1-XS-3	-0.20	0.11	2.50	0.09	-1.71	0.80
Nodule 1-XS-4	-0.33	0.11	2.20	0.11	-1.10	0.64
Nodule 1-XS-5	-0.59	0.11	2.29	0.08	-1.17	0.54
Nodule 1-XS-6	-0.87	0.11	2.13	0.11	-1.28	0.55
Nodule 1-XS-7	-1.28	0.11	2.10	0.11	-0.76	0.57
Nodule 1-XS-8	-0.97	0.13	2.58	0.12	-1.27	0.59
Nodule 1-XS-9	-1.43	0.18	2.58	0.12	-0.49	0.87
Nodule 1-XS-10	2.47	0.11	0.17	0.10	0.48	0.55
Nodule 1-XS-11	1.10	0.11	0.23	0.09	0.62	0.59
Nodule 1-XS-12	-0.23	0.15	0.14	0.13	0.37	0.61
Nodule 1-XS-13	0.54	0.12	0.18	0.10	1.36	0.54
Nodule 1-XS-14	1.63	0.11	1.04	0.08	0.27	0.53
Nodule 1-XS-15	1.52	0.11	0.98	0.10	0.49	0.53
Nodule 1-XS-16	1.33	0.12	0.79	0.12	0.08	0.55
Nodule 1-XS-17	1.59	0.11	-0.05	0.10	0.83	0.54
Nodule 1-XS-18	1.11	0.12	-0.21	0.12	1.24	0.55
Nodule 1-XS-19	0.12	0.12	0.33	0.13	0.20	0.55
Nodule 1-XS-20	0.21	0.12	0.22	0.08	1.18	0.55
Nodule 1-XS-21	1.15	0.12	0.24	0.12	1.38	0.54
Nodule 1-XS-22	2.19	0.16	0.14	0.12	0.32	0.58
Nodule 1-XS-23	-0.54	0.11	2.75	0.10	-1.42	0.63
Nodule 1-XS-24	-0.73	0.12	2.55	0.10	-1.01	0.59
Nodule 1-XS-25	-0.77	0.11	2.30	0.10	-0.56	0.72
Nodule 1-XS-26	-1.23	0.11	2.13	0.11	-0.76	0.57
Nodule 1-XS-27	-0.84	0.14	2.06	0.11	-0.76	0.55
Nodule 1-XS-28	-0.76	0.11	2.18	0.10	-1.65	0.52
Nodule 1-XS-29	-0.45	0.11	2.45	0.11	-0.84	0.52

Sample	$\delta^{34}S_{(VCDT)}$ (‰)	2σ (‰)	$\Delta^{33}S$ (‰)	2σ (‰)	$\Delta^{36}S$ (‰)	2σ (‰)
Nodule 1-XS-30	-0.87	0.14	3.26	0.11	-2.09	0.56
Nodule 1-XS-31	0.45	0.11	3.61	0.09	-1.79	0.52
Nodule 1-XS-32	0.78	0.11	3.51	0.08	-2.21	0.53
Nodule 2-XS-1	-0.53	0.12	2.77	0.09	-1.79	0.55
Nodule 2-XS-2	-0.64	0.12	2.84	0.08	-1.26	0.57
Nodule 2-XS-3	-0.21	0.11	2.60	0.09	-1.12	0.57
Nodule 2-XS-4	2.47	0.12	0.66	0.13	0.03	0.61
Nodule 2-XS-5	1.48	0.11	-0.14	0.08	1.37	0.56
Nodule 2-XS-6	0.13	0.19	0.04	0.16	1.61	0.73
Nodule 2-XS-7	0.45	0.11	0.10	0.08	1.08	0.68
Nodule 2-XS-8	0.46	0.14	0.13	0.14	1.31	0.64
Nodule 2-XS-9	2.11	0.11	-0.12	0.08	1.27	0.78
Nodule 2-XS-10	2.20	0.11	-0.24	0.13	1.09	0.55
Nodule 2-XS-11	1.77	0.11	-0.58	0.11	1.88	0.55
Nodule 2-XS-12	1.36	0.12	-0.02	0.09	0.89	0.64
Nodule 2-XS-13	2.68	0.11	0.54	0.10	0.88	0.56
Nodule 2-XS-14	-0.26	0.11	2.91	0.08	-1.41	0.73
Nodule 2-XS-15	-0.26	0.11	2.70	0.08	-1.81	0.55
Nodule 2-XS-16	-1.15	0.11	2.35	0.09	-0.98	0.55
Nodule 2-XS-17	-1.03	0.11	2.17	0.12	-1.22	0.58
Nodule 2-XS-18	-1.08	0.11	2.05	0.10	-1.01	0.65
Nodule 2-XS-19	-0.92	0.11	2.25	0.12	-1.38	0.55
Subhedral pyrite-1	4.76	0.11	0.74	0.14	-0.07	0.52
Subhedral pyrite-2	4.94	0.11	0.50	0.08	0.06	0.60
Subhedral pyrite-3	4.18	0.11	1.23	0.10	-0.05	0.63
Subhedral pyrite-4	5.03	0.11	0.45	0.11	0.49	0.59
Subhedral pyrite-5	3.55	0.11	0.51	0.08	0.35	0.52
Subhedral pyrite-6	3.91	0.11	1.22	0.08	-0.40	0.53
Subhedral pyrite-7	5.26	0.11	0.46	0.08	0.20	0.66

Sample	$\delta^{34}S_{(VCDT)}$ (‰)	2σ (‰)	$\Delta^{33}S$ (‰)	2σ (‰)	$\Delta^{36}S$ (‰)	2σ (‰)
Subhedral pyrite-9	5.25	0.11	0.44	0.12	0.03	0.66
Subhedral pyrite-10	4.61	0.11	0.77	0.09	-0.34	0.52
Subhedral pyrite-11	4.17	0.11	1.10	0.08	-1.07	0.52
Subhedral pyrite-12	4.08	0.11	1.27	0.08	-0.15	0.52
Subhedral pyrite-13	3.73	0.11	0.81	0.08	-0.23	0.52
Subhedral pyrite-14	5.10	0.11	0.35	0.10	0.34	0.52
Subhedral pyrite-15	4.83	0.11	0.68	0.08	-0.05	0.52
Subhedral pyrite-16	5.23	0.11	0.43	0.08	0.18	0.52
Subhedral pyrite-17	3.93	0.11	1.23	0.08	-0.87	0.53
Subhedral pyrite-18	4.60	0.11	1.02	0.10	-0.05	0.63
Subhedral pyrite-19	4.66	0.11	0.97	0.08	-0.72	0.53